Surfaces, Interfaces, and Applications

Dropwise Condensation on Multi-scale Bioinspired Metallic Surfaces with Nano-Features

Daniel Orejon, Alexandros Askounis, Yasuyuki Takata, and Daniel Attinger

ACS Appl. Mater. Interfaces, **Just Accepted Manuscript** • DOI: 10.1021/acsami.9b06001 • Publication Date (Web): 10 Jun 2019

Dropwise Condensation on Multi-scale Bioinspired Metallic Surfaces with Nano-Features

Daniel Orejon[1,2*], Alexandros Askounis[2,3], Yasuyuki Takata[2,4], Daniel Attinger[5]

[1]Institute for Multiscale Thermofluids, School of Engineering, The University of Edinburgh, EH9 3FD, Scotland, UK

[2]International Institute for Carbon-Neutral Energy Research (WPI-I2CNER), Kyushu University, 744 Motooka, Nishi-ku, Fukuoka 819-0395, Japan

[3]Engineering, Faculty of Science, University of East Anglia, Norwich, NR5 7TJ, UK

[4]Department of Mechanical Engineering, Thermofluid Physics Laboratory, Kyushu University, 744 Motooka, Nishi-ku, Fukuoka 819-0395, Japan

[5]Deparment of Mechanical Engineering, Iowa State University, Ames, USA

Abstract

Non-wetting surfaces engineered from intrinsically hydrophilic metallic materials are promising for self-cleaning, anti-icing and/or condensation heat transfer applications where the durability of the coating is an issue. In this work, we fabricate and study the wetting behaviour and the condensation performance on two metallic non-wetting surfaces with varying number and size of the roughness tiers without further hydrophobic coating procedure. On one hand, the surface resembling a rose petal exhibits a sticky non-wetting behaviour as drops wet the microscopic roughness features with the consequent enhanced drop adhesion, which leads to filmwise condensation. On the other hand, the surface resembling a lotus leaf provides super-repellent non-wetting behaviour prompting the continuous nucleation, growth and departure of spherical drops in a dropwise condensation fashion. On a lotus leaf surface, the third nano-scale roughness tier (created by chemical oxidation) combined with ambience exposure prompts the growth of drops in the Cassie state with the benefit of minimal condensate adhesion. The two different condensation behaviours reported are well supported by a drop surface energy analysis, which accounts for the different wetting performance and the surface structure underneath the condensing drops. Further, we coated the above-mentioned surfaces with polydimethylsiloxane surfaces, which resulted in filmwise condensation due to the smoothening of the different roughness tiers. Continuous dropwise condensation on a hierarchical bioinspired lotus leaf metallic surface without the need for a conformal hydrophobic coating is hence demonstrated, which offers a novel path for the design and manufacture of non-coated metallic super-repellent surfaces for condensation phase change applications, amongst others.

Keywords: dropwise condensation, condensation heat transfer, copper oxide nanostructures, bioinspired hierarchical surfaces, multi-scale metallic surface, wetting, atmosphere-mediated hydrophobicity

INTRODUCTION

Condensation phase change has important implications in electricity generation,[1] air conditioning,[2] water treatment,[3] fog harvesting,[4] and heat management applications,[5] amongst others. The two widely accepted mechanisms for condensation are filmwise condensation occurring typically on a high surface energy hydrophilic surface, and dropwise condensation typically developing: in the presence of a low surface energy hydrophobic promoter,[6-7] upon adsorption of carbon rich contaminants,[8-10] and/or in the presence of re-entrant structures.[11] The occurrence of the condensate in a dropwise manner provides up to 5 to 10 times greater heat transfer coefficients when compared to filmwise condensation due to the easiness of the former to shed the condensate.[12-14] The continuous shedding of the condensate results in new refreshed area available for re-nucleation and growth of small drops, providing enhanced heat transfer performance when compared to filmwise.[7, 15] In addition, the coexistence of dropwise and filmwise condensation has been recently reported and its greater heat transfer performance when compared to solely filmwise condensation has been demonstrated.[16-18]

In the past decade, researchers have focused their efforts on the design of condensation surfaces capable of performing in a continuous dropwise condensation manner. To this end, flat hydrophobic surfaces and superhydrophobic surfaces that combine micro- and/or nano-structures with the addition of a hydrophobic coating, have been proposed for their excellent condensation and self-cleaning properties. A 30% enhancement in the condensation heat transfer coefficient has been reported on nano-structured superhydrophobic surfaces when compared to smooth hydrophobic ones.[6, 19] The greater heat transfer performance was attributed to the ability of superhydrophobic surfaces to prompt the self-removal of sub-millimetre drops via drop shedding by gravity and/or by coalescence-induced drop-jumping.[6, 20-21] Hence the surface is refreshed for condensate drop re-nucleation and growth, which is characteristic of high heat transfer. In the presence of micro-structured surfaces, the self-dewetting transition of drops condensing between superhydrophobic micro-pillars toward their tops has been recently reported.[22] This self-dewetting transition is induced by a difference of Laplace pressure arising within the drop, *i.e.*, between the bottom and the top of the drop, which brings the condensate to a lower energy of adhesion state facilitating drop self-removal.[22] More recently, Sharma *et al*. have induced the spontaneous navigation of drops growing between micro-cavities towards the surface top.[23] This spontaneous navigation is also attributed to the imbalance in Laplace pressure exerted within the drop by the confined geometry of the superhydrophobic cavities.[23] Further, to ease drop mobility, similar imbalance of outward Laplace pressure has been exploited in the presence of micro-grooves on superhydrophobic

copper nanowire surfaces.[24] When looking into a solely nanostructured surface, Cha *et al.* demonstrated the feasibility of coalescence-induced drop-jumping of submicrometre drops on superhydrophobic carbon nanotubes.[25] More recently, Mulroe *et al.* provided the first rational guidelines to control and tune coalescence-induced drop-jumping on superhydrophobic nanopillared surfaces.[26] In addition to the abovementioned works, the use of a porous biphilic nanostructure where the hydrophobic layer is utilized to confine the condensate within the nanostructures has been recently reported.[18] Nonetheless, despite the state-of-art hydrophobic and superhydrophobic surfaces with unique functionalities and enhanced condensation performance reported above, the need for a hydrophobic coating render such surfaces impracticable in certain environments and/or for long-term applications.[27-29]

Besides the state of the art superhydrophobic surfaces reported above, structured bioinspired surfaces have also been further proposed for their unique surface structures and functionalities. Bioinspired surfaces have been exploited in light of their excellent anti-icing, fog harvesting and for condensation heat transfer applications, amongst others.[30-32] Soft-lithography,[33-34] precise moulding technique followed by self-assembly,[35] zinc film electrodeposition,[36] annealing and electrodeposition of copper,[37] nanoparticle deposition by laser irradiation,[38] inkjet printing,[39] spin coating,[40] spray deposition or embedding of hydrophobic silica nanoparticles,[41-42] and chemical texturing,[6, 43-44] are some of the approaches adopted for the design and fabrication of such bioinspired surfaces. However, for successful non-wetting properties as well as for the occurrence of continuous dropwise condensation, most of these approaches require the addition of a hydrophobic silanes or the deposition of polymeric hydrophobic nanoparticles.[38-39, 41-42, 45] Top down texturing and structuring of bulk polymeric materials can also promote dropwise behaviour, however the thermal conductivity of these polymers is dramatically lower when compared to metal ones.[34, 40] To counteract the above mentioned drawbacks, bioinspired non-wetting hydrophobic and superhydrophobic surfaces engineered from purely metallic materials such as copper or aluminium without the need for a polymeric hydrophobic coating have been recently demonstrated.[35, 43-44] Nonetheless, the occurrence of sustained dropwise condensation on metallic surfaces is yet to be demonstrated.

Metal, metal oxides and rare earth oxides engineered surfaces have received increasing attention due to the unique potential to transition from hydrophilic to hydrophobic and/or to superhydrophobic wettability upon ambient exposure. In the case of rare earth oxides, the wettability transition is primarily due to the absorption of volatile organic compounds (VOCs) present in the ambient.[9, 46-47] Whereas in the case of metal and metal oxides (such as copper and copper oxide) upon exposure to the ambient, the transition from wetting to non-wetting is

a consequence or a combination of the following factors; deoxidation of the copper oxide into cuprous oxide,[48] further physical adsorption of oxygen,[37] and/or adsorption of volatile organic compounds (VOCs).[10, 49] Such transition in surface wettability resulting in superhydrophobicity of metallic surfaces has been recently reported on: nanowire films,[48] hierarchical micro-/nano-structures,[10, 37, 50] hierarchical multi-scale roughness surfaces,[44] and/or metal foams.[49] The hydrophobicity or superhydrophobicity of such copper and copper oxide surfaces, without the assistance of an additional polymeric hydrophobic coating should, in turn lead to continuous dropwise condensation. In the particular case of rationally designed micro-/nano-structured copper oxide surfaces, coalescence-induced droplet-jumping on a horizontal surface and under prolonged exposure to steam have been recently reported.[10] In this work, we rather focus on addressing the importance of the different tiers of roughness on the coalescence and on the condensation behaviour (mainly on droplet growth, coalescence and shedding) on a rose petal and on a lotus leaf bioinspired surfaces.

Two metallic bioinspired copper surfaces were fabricated by easy and scalable stochastic chemical texturing which, upon interactions with liquid drops, mimics the sticky and the super-repellent non-wetting behaviours of a rose petal (RP) and of a lotus leaf (LL), respectively, as in the work of Frankiewicz and Attinger.[44] In the case of a metallic RP, the single chemical etching fabrication step confers the metallic surface with two levels of topographical micro-features varying in size (two tiers of roughness) as in the natural rose petal sample.[51] Whereas a metallic LL was subjected to an additional oxidation step conferring this surface with an additional third nano-scale tier of roughness as in the natural lotus leaf sample.[52] Further, polydimethylsiloxane (PDMS) coated counterparts as RP_{PDMS} and LL_{PDMS} were prepared and characterized to assess the influence of the polymeric coating on the condensation behaviour of the inherently super-repellent surfaces. Surface structure and wettability for all four surfaces were characterized by means of Scanning Electron Microscopy SEM and macroscopic contact angle measurements. In addition, the transition from wetting to non-wetting behaviour function of ambient exposure coupled with the chemical characterization of our metallic RP and LL surfaces is presented to support earlier reported hydrophilicity to hydrophobicity and/or to superhydrophobicity transitions on such copper oxide surfaces.[10, 48-49] Last, all four surfaces were subjected to dynamic experimental observations of condensation phase change at both the macro- and the micro-scale.

The third nano-scale tier of roughness coupled with the unique wetting transition from hydrophilic to superhydrophobic upon exposure to the ambient taking place on copper and copper oxide, are responsible for the different final condensation mechanisms reported when

comparing dropwise condensation on a LL to filmwise condensation on a RP. Upon PDMS addition, the non-uniformity of the PDMS coating and the smoothening of the sharp copper oxide features (third roughness tier) result on eventual filmwise condensation on both RP_{PDMS} and LL_{PDMS}. To further demonstrate the different condensation mechanisms, *i.e.*, dropwise condensation *vs.* filmwise condensation, depending on the sticky and super-repellent non-wetting behaviours on a RP and on a LL, respectively, we present a surface energy analysis based on the energy of adhesion and on the excess of surface energy of the drop. In addition, quantification on the experimental observations as sphericity of the coalescing drops before and after coalescence, as well as the evolution of the surface coverage remarkably agree with the proposed energy analysis.

RESULTS AND DISCUSSION

Substrate Characterization

Two metallic surfaces resembling the sticky non-wetting behaviour of a rose petal (RP) and the super-repellent non-wetting behaviour of a lotus leaf (LL) were fabricated following the same easy and scalable etching and oxidation procedures reported in Ref. 44 (More details on the fabrication procedure and characterization of the surfaces can be found in the Materials and Methods Section, in the accompanying Supporting Information and in Ref. 44).[44] The low temperatures required during etching (ambient temperature) and during oxidation (ca. 65 ^{0}C) coupled with the low quantity of reagents needed make the reported fabrication technique easy scalable for mass production ideal for domestic air conditioning condensers. In addition, RP_{PDMS} and LL_{PDMS} counterparts were prepared by vapour deposition of poly(dimethylsiloxane) (PDMS).[53-54] The intrinsic surface wettability upon PDMS vapour deposition procedure is that of the PDMS on a flat surface, *i.e.*, $\theta_{i,PDMS} = 112° \pm 4°$. To further confirm the successful replication of the surface structure and that of the non-wetting behaviours, all surfaces were characterized by Scanning Electron Microscopy (SEM) and macroscopic contact angle measurements.

The surface structure of a RP, a LL and their PDMS counterparts (RP_{PDMS} and LL_{PDMS}) was assessed in an Environmental Scanning Electron Microscope (ESEM, Versa 3D, FEI Co., USA). Figure 1 presents SEM snapshots at different magnifications for all four samples:

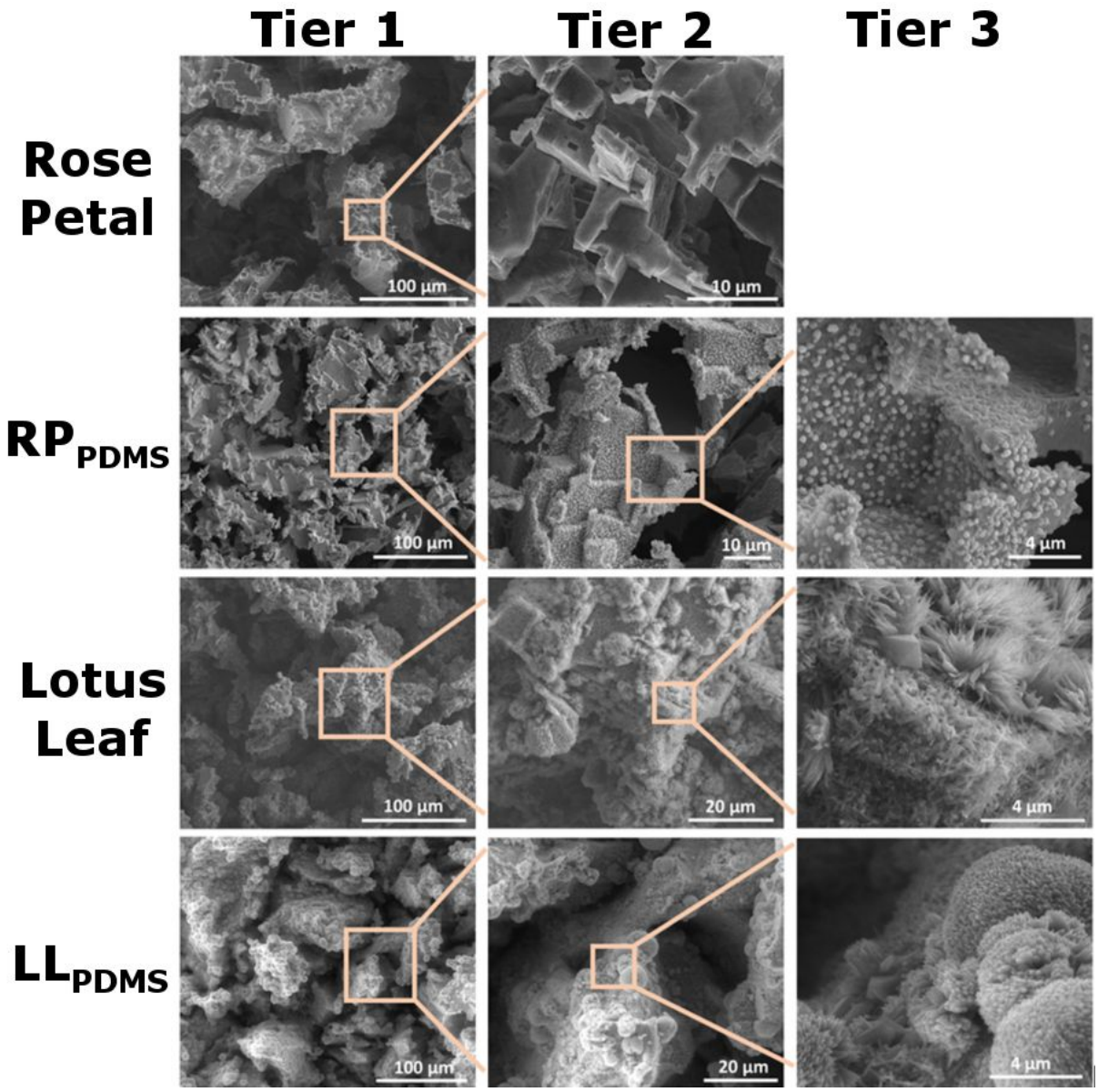

Figure 1 - SEM snapshots of the multi-scale surface features observed on a RP, a LL and on their PDMS coated counterparts RP_{PDMS} and LL_{PDMS}. Special emphasis is given to the different tiers of roughness.

The surface structure of a metallic RP consists of two tiers of roughness, the main one Tier 1 being large pillars with lateral dimensions of approximately 50 – 100 µm and 200 – 300 µm in height, while a Tier 2 consists of features with dimensions smaller than 10 µm that resemble stacked "Lego bricks". In the case of the $RP_{PDMS,}$ the addition of the PDMS results in the formation of a third tier of roughness of smooth rounded globules with average diameter ~ 400 nm, *i.e.*, Tier 3. The surface structure of a metallic LL is shaped by the same two micro-scale tiers of roughness with an additional oxide nano-scale Tier 3. The oxidation procedure yields sharp nano-scale fibrils/spears with diameters in the order of 10 – 100 nm, and 100 – 300 nm

in length, *i.e.*, Tier 3. In occasions, nano-scale fibrils or spears are arranged in bouquets of 4 – 5 μm. The addition of PDMS to a LL, *i.e.*, LL_{PDMS}, resulted on the smoothening of the Tier 3 fibrils tops while filling the gaps between the nano-scale fibrils/spears, which effectively increase the solid fraction. The height of the micro-structures h is obtained from 3D optical laser scanning microscopy as 241 ± 27 μm (see 3D optical laser scanning microscopy snapshots from a metallic rose petal in Figure S1 in the accompanying Supporting Information S3). The height of the micro-structures h was obtained from the average S_z estimated from 3 different independent 3D optical laser scanning microscopy areas. S_z is defined as the sum of the largest peak and height and the largest pit depth within the analysed surface area.

Next, the accepted sticky and the super-repellent non-wetting behaviours of the fabricated metallic RP and LL earlier reported in literature are confirmed.[44] The equilibrium contact angle, θ_0 (deg), advancing contact angle, θ_a (deg), receding contact angle, θ_r (deg), and contact angle hysteresis, CAH = θ_a - θ_r (deg), were assessed by a custom-built contact angle goniometer. To preserve the wetting properties as per fabricated, prior to contact angle measurements, surfaces were rinsed with deionized water and dried with a stream of filtered air. Contact angle values are presented in Table 1:

Table 1 – Equilibrium contact angle, θ_0 (deg), advancing contact angle, θ_a (deg), receding contact angle, θ_r (deg), and contact angle hysteresis, CAH (deg), for each surface.

Sample	Equilibrium contact angle, θ_0 (deg)	Advancing contact angle, θ_a (deg)	Receding contact angle, θ_r (deg)	Contact angle hysteresis, CAH = θ_a - θ_r (deg)	Wetting Behaviour
RP	141° ± 2°	148° ± 5°	101° ± 13°	47°	Sticky non-wetting[55]
RP_{PDMS}	145° ± 5°	158° ± 6°	103° ± 8°	55°	Sticky non-wetting
LL	134° ± 3°	138° ± 5°	134° ± 5°	4°	Super-repellent non-wetting[44, 56]
LL_{PDMS}	143° ± 4°	147° ± 6°	125° ± 9°	22°	Sticky non-wetting

Wetting to Non-wetting Transition Characterization

The transition from wetting to non-wetting and/or from hydrophilic/superhydrophilic to hydrophobic/superhydrophobic upon surface exposure to the ambience has been reported on rare earth oxides,[46-47] copper foams,[49] nanowire films,[48] and micro-/nano-structured copper/copper oxide surfaces.[10, 50] In order to demonstrate the wetting to non-wetting transition

and the self-healing nature to plasma etching of the rose petal (RP) and lotus leaf (LL) copper and copper/copper oxide surfaces reported here. Further characterization of the wettability and of the surface chemical composition at different intervals of ambient exposure after cleaning the surfaces with oxygen plasma was carried out. RP and LL surfaces were cleaned in a plasma etching system FA-1 from SAMCO (Japan). More details on the cleaning procedure can be found in the Materials and Methods and in Section S5 of the Supporting Information. Then, the advancing contact angles, θ_a (deg), on a RP and on a LL surfaces were measured at $t = 0$ hours, 4 hours, 16 hours, 36 hours, 108 hours (4 days and a half) and 504 hours (3 weeks) with $t = 0$ hours as the time right after oxygen plasma cleaning. The surfaces were then exposed to laboratory environment located in Room 402 at the International Institute for Carbon-Neutral Energy Research at Kyushu University, Japan (33° 35' 49"N, 130° 13' 32" E). More details on the advancing contact angles, θ_a (deg), including the measured values along with their standard deviation can be found in Table S1 in the accompanying Supporting Information. Furthermore, we also analysed the chemical composition, atomic %, of the surfaces at the same exposure times within the first week, *i.e.*, $t = 0$ hours, 4 hours, 16 hours, 36 hours and 108 hours (4 days and a half). The chemical composition at the outermost surface was analysed by Energy Dispersive X-Ray Spectroscopy (EDS) in a Field Emission SEM JSM-7900F from JEOL (Tokyo, Japan). We note here that we did choose Energy Dispersive X-Ray Spectroscopy (EDS) over X-Ray Photoelectron Spectroscopy (XPS) since the Scanning Electron Microscopy (SEM) built-in capability of the SEM JSM-7900F allows for the chemical characterization of the micro- and/or the nano-structures locally, rather than providing an area were both the chemical composition of the micro- and the nano-structures are averaged (see Figure S9 and S10 in the accompanying Supporting Information). The main elements analysed were carbon, oxygen and copper, which accounted for more than 96% of the composition of the elements present at the surface. More details and the reported values of the chemical composition on a RP and on a LL can be found in Table S2 and Table S3 in Section 6 of the accompanying Supporting Information. To summarize the experimental results on the wetting and surface chemistry transitions upon ambient exposure, we now present the advancing contact angle, θ_a (deg), and the surface chemical composition for carbon, oxygen and copper, versus exposure time for a RP and for a LL in Figure 2a and Figure 2b:

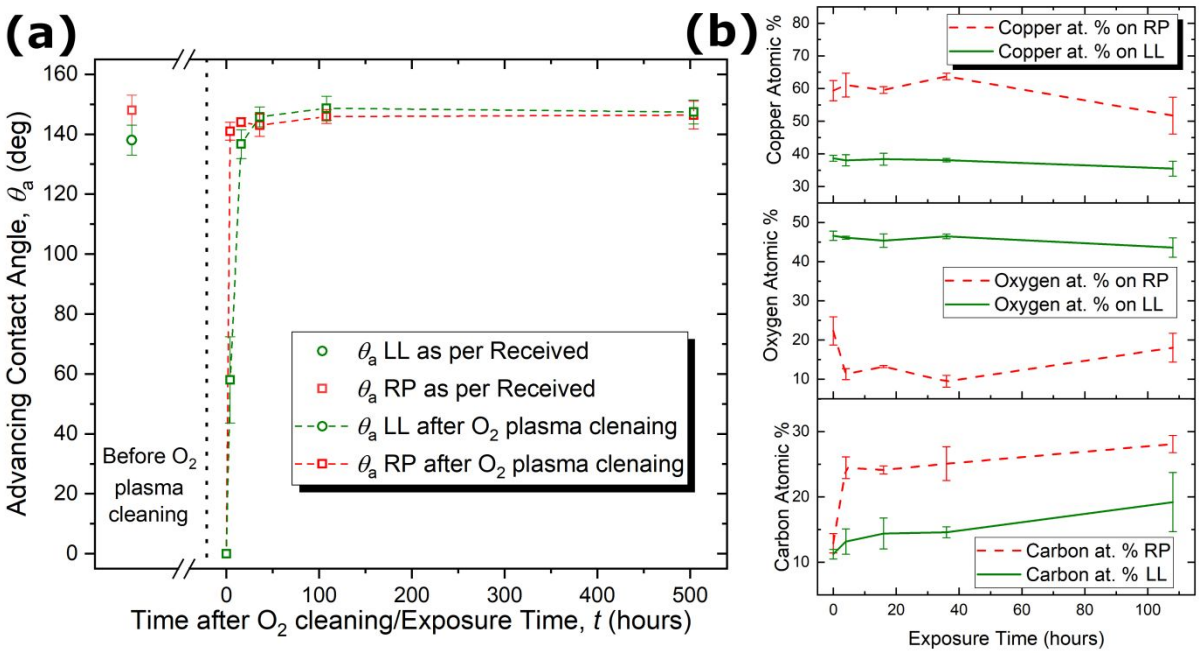

Figure 2 – (a) Advancing contact angle, θ_a (deg), as per received (left of dashed line) and for $t = 0$, 4, 16, 36, 108 and 504 hours exposure to laboratory environment, with $t = 0$ as right after oxygen plasma cleaning (right of dashed line), for (red empty squares) a RP and for (green empty circles) a LL. (b) surface chemical composition in atomic % for (top) copper, (middle) oxygen and (bottom) carbon versus exposure time, t (hours), for (dashed lines) a RP and for (solid line) a LL. Error bars represent the standard deviation of at least three independent measurements.

Right after cleaning the surfaces with oxygen plasma, upon droplet sessile deposition on both surfaces, droplets completely spread evidencing the superhydrophilic nature of the prepared surfaces before being exposed to the ambient. Once the surfaces are being exposed to ambient environment, in this case laboratory conditions, both surfaces start to recover their non-wetting properties. On one hand, in the case of a micro-structured RP surface, the nature of the copper outermost surface enables the non-wetting characteristic of the surface within 4 hours upon exposure. Then the advancing contact angle, θ_a (deg), continues increasing slightly until a plateau is reached at ca. 146^0 after several days as it can be observed from Figure 2a. The qualitative increase in the advancing contact angle, θ_a (deg), can be correlated with the qualitative increase in the carbon adsorbed at the copper surface masking the initial presence of oxygen groups (see Figure 2b), which eventually provide the reported non-wetting characteristics.[10, 46] On the other hand, in the case of a hierarchical LL surface, the copper oxide nano-structures take longer to provide the required intrinsic hydrophobicity in order to enable the non-wetting nature of the surface upon ambient exposure as per the contact angle in the

wetting regime reported after 4 hours of exposure (Figure 2a). Nonetheless, LL surfaces are able to attain an advancing contact angle, θ_a (deg), as high as 136^0 within 1 day of exposure and increases up to 147^0 after several days. The slower carbon adsorption on the copper oxide nano-structures on a LL when compared to the quicker carbon adsorption taking place on the copper micro-structured RP is reported in Figure 2b, which is in agreement with the evolution of the advancing contact angle, θ_a (deg), reported in Figure 2a. The self-healing nature and the non-wetting transition dynamics upon chemical etching by oxygen plasma is then demonstrated and distinction is made between the different nature of the outermost surface of the RP and that of the LL based on the tier of roughness. Moreover, we stress here on the self-healing nature upon ambient exposure of the LL surface with an advancing contact angle, θ_a (deg), greater than the one reported on as per received surfaces (Figure 2a). Accelerated volatile organic compound (VOC) deposition leading to greater advancing contact angles, θ_a (deg), when compared to as per fabricated surfaces is in agreement with the work of Yan et al..[10]

Experimental Observations at the Micro-scale

Condensation experimental observations by optical microscopy were carried out inside an environmental chamber PR-3KT from ESPEC Corp. (Japan) and were recorded using a high-resolution microscopy zoom lens Keyence VH-Z500R (Japan) attached to a CCD camera Sentech STC-MC152USB (Japan). The condensation conditions (see Materials and Methods Section) were as follows: ambient temperature $T_{amb} = 30 \pm 2$ °C and relative humidity $RH = 80 \pm 5\%$ with a surface temperature $T_{wall} = 10 \pm 1$ °C, providing a degree of supersaturation of approximately 2.78 ± 0.5. Experimental and supersaturation conditions are in agreement with those reported earlier in the work of Zhang *et* al. for the study of coalescence-induced droplet-jumping on micro-/nano- and nano-structured superhydrophobic surfaces.[57] We stress here that prior to experimental observations, all surfaces were rinsed with deionized water and dried with a stream of filtered air. Cleaning with deionized water was adopted aiming to preserve the non-wetting characteristics of the surface as per fabricated.[44] The use of sonication with organic solvents and/or the cleaning with oxygen plasma was avoided since both procedures have been demonstrated to induce different wetting nature of such copper oxide surfaces.[10, 48-50] More details on the equipment and on the methodology followed can be found in the Materials and Methods Section and/or in the accompanying Supporting Information. Characteristic snapshots

acquired by optical microscopy during experimental observations on a metallic RP, RP_{PDMS}, LL and LL_{PDMS} at different condensation times are presented in Figure 3.

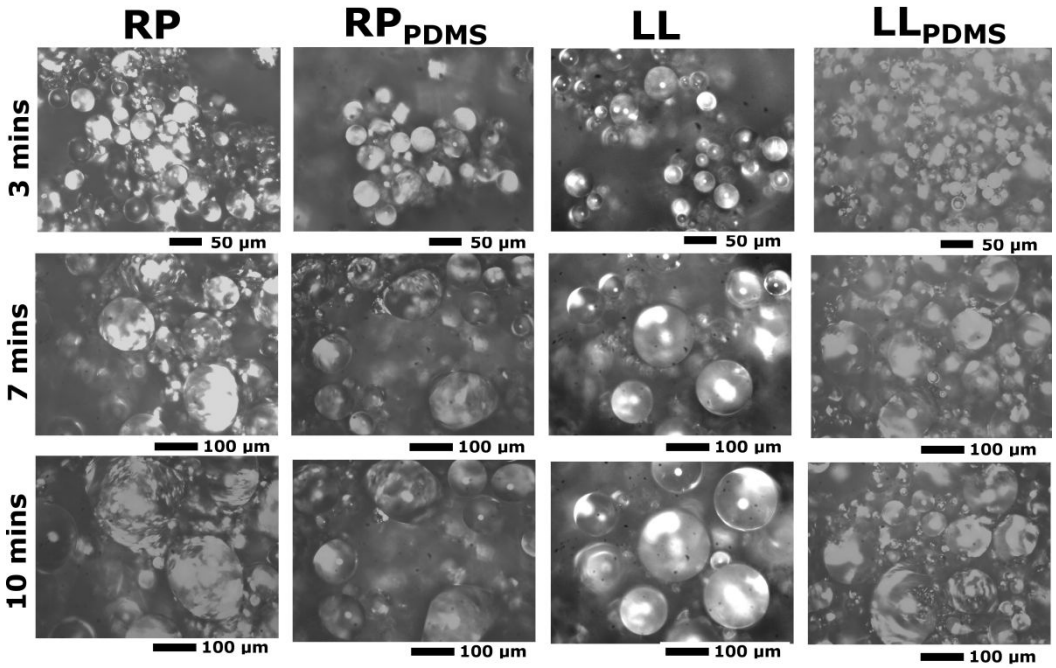

Figure 3 - Representative optical microscopy snapshots of condensation on metallic RP (see Supporting Information, Video S1), metallic RP_{PDMS} (see Supporting Information, Video S2), metallic LL (see Supporting Information, Video S3) and metallic LL_{PDMS} surfaces (see Supporting Information, Video S4) at (top) t = 3 minutes, (middle) t = 7 minutes and (bottom) t = 10 minutes with t = 0 minutes as the observed onset of nucleation. Scale bars are 50 and 100 µm.

At early stage of condensation, *i.e.*, 3 minutes (Figure 3, top row), rounded/spherical drops nucleate and grow to sizes in the order of tens of µm on all four surfaces. Since the different tiers of roughness are built up on top of each other, drop nucleation and growth typically occur on the uppermost roughness tier. On a metallic RP drops nucleate and grow on the micro-scale roughness Tier 2, whereas on a metallic LL drops nucleate and grow on top and/or within the nano-scale roughness Tier 3. Drops displaying a 2D rounded/circular shape (top view) can be approximated to spherical cap shape; hence, for simplicity we define sphericity as how close the drops approximate a circle, *i.e.*, circularity. Darker regions in Figure 3 depict substrate locations below the field-of-view of the optical microscopy.

As condensation develops, drops grow bigger and begin to coalesce with each other. For condensation times *ca.* 7 minutes (Figure 3, middle row), representative snapshots on a RP, a RP_{PDMS} and a LL_{PDMS} show that the shape of the drops exhibit a deviation from rounded/spherical. On a RP, on a RP_{PDMS} and on a LL_{PDMS}, drops in the order of hundreds of

μm can no longer maintain their initial spherical shape throughout growth and/or coalescence. Deviations from spherical shape in the case of a RP, a RP_{PDMS} and a LL_{PDMS} become more evident after 10 minutes from the onset of condensation (Figure 3, middle and bottom rows). Whereas in the case of a LL, remarkably rounded/spherical drops are reported throughout both growth and coalescence and for the entire duration of the optical microscopy experimental observations (Figure 3 bottom). Optical microscopy observations on a RP, on a RP_{PDMS}, on a LL and on a LL_{PDMS} are included in the accompanying Supporting Information in Videos S1, S2, S3 and S4, respectively.

Mechanisms of Drop Coalescence

Next, we focus our attention on the different drop shapes adopted upon coalescence depending on the surface studied. Figure 4 shows characteristic optical microscopy snapshots before and after drop coalescence at earlier (3 minutes) and at later (7 minutes) condensation times.

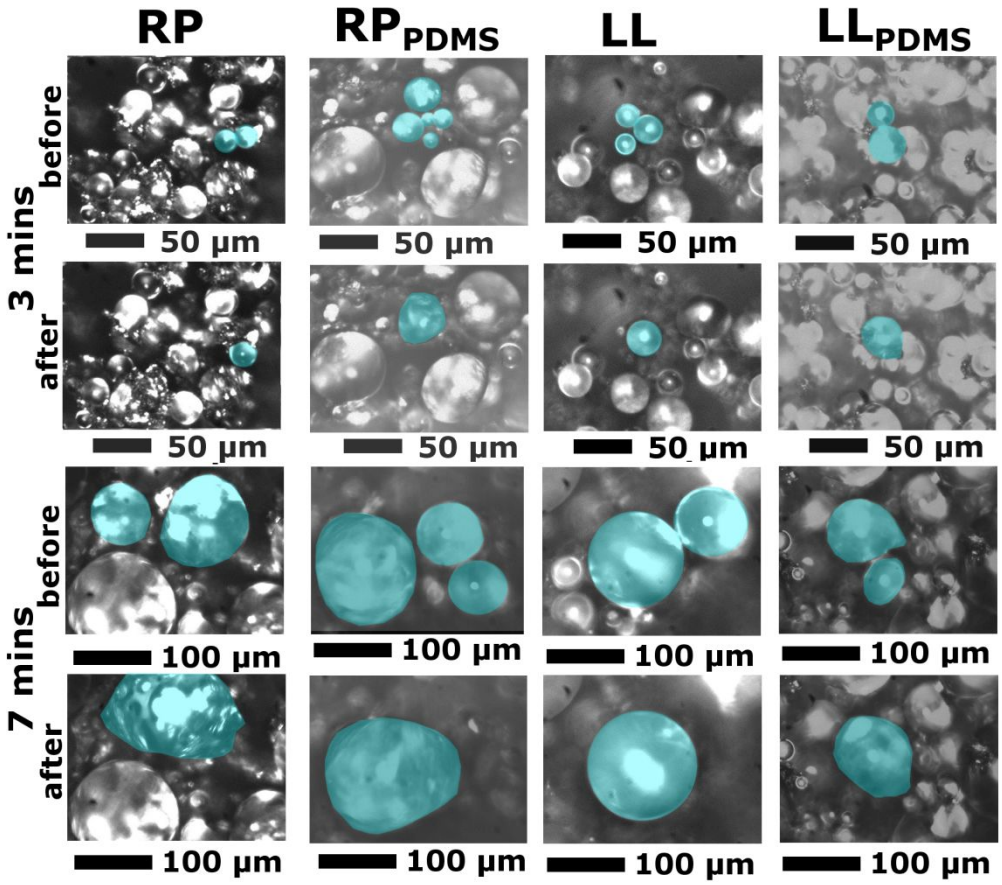

Figure 4 - Characteristic optical microscopy snapshots before and after coalescence on a metallic RP, a metallic RP_{PDMS}, a metallic LL and a metallic LL_{PDMS} surfaces at (top) *ca.* 3 minutes and (bottom) *ca.* 7 minutes. False blue color has been applied to readily identify the drops involved in the coalescence events and the new coalesced/merged drops. Scale bars are 50 and 100 μm.

At the earlier stages of condensation ca. 3 minutes (Figure 4, top rows), new merged drops (with sizes in the same order of magnitude as Tier 2) are able to maintain a nearly circular/spherical shape throughout growth and coalescence on all four surfaces. Nonetheless, a slight deviation from spherical begins to be noticeable for merged drops in the case of RP, a RP_{PDMS} and a LL_{PDMS}. As the condensing drops grow, at ca. 7 minutes (Figure 4, bottom rows), new merged drops display irregular and elongated shapes that clearly deviate from that of spherical cap in the case of a RP, a RP_{PDMS} and a LL_{PDMS} surfaces. Upon coalescence of drops with sizes of tens of micrometers (bigger than the characteristic size of the Tier 2 of roughness), the drop contact line is unable to depin and the new merged drops stretch. On a LL, however, the contact line does depin from the Tier 3 nano-features and new merged drops maintain their spherical shape throughout drop growth and multiple coalescing events.

In order to provide further insights on the shape of the drops throughout growth and coalescence the degree of sphericity/circularity before and after coalescence, *i.e.*, for coalescing and for merged drops respectively, is measured and averaged from 30 to 60 different coalescing events for each of the four samples studied. The size and the circularity/sphericity of the drops were extracted from optical microscopy experimental observations by manually fitting the shape of the drop using ImageJ.[58] Moreover, the sphericity difference defined as the drop sphericity before coalescence minus the drop sphericity of the new merged drop is also presented along for all four samples. Then, the average sphericity for coalescing and for merged drops as well as the average drop sphericity difference, are presented in Figure 5 for RP, LL, RP_{PDMS} and LL_{PDMS} at drop size intervals of 20 μm:

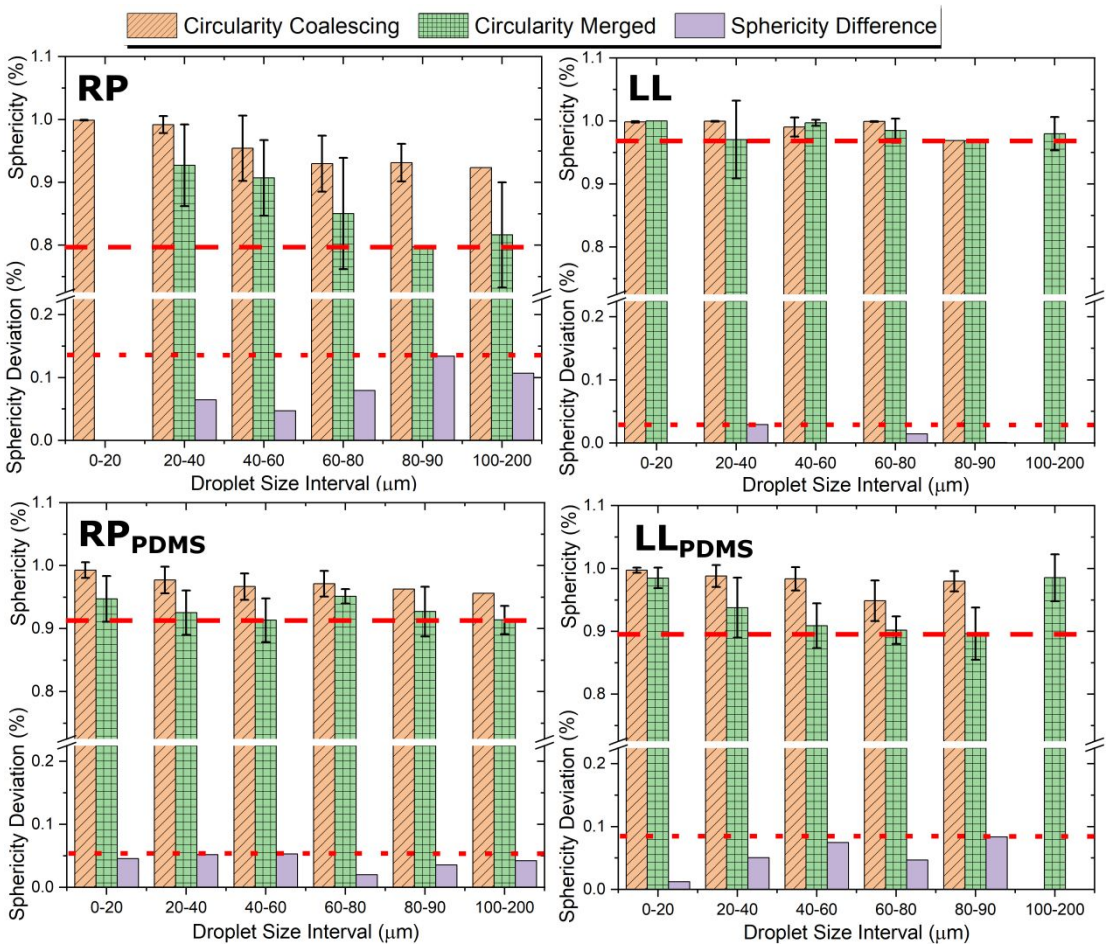

Figure 5 – Average drop sphericity (diagonal pattern) before coalescence, (checker board) after coalescence and (plain) difference (drops sphericity before coalescence minus the drop sphericity of the new merged drop) for RP, LL, RP_{PDMS} and LL_{PDMS}. Dashed lines show the minimum sphericity of merged drops and dotted lines show the maximum sphericity difference.

From Figure 5, on one hand, on a RP the degree of sphericity noticeably decreases as the size of the drops increases for either coalescing drops or new merged drops. The deviation from spherical cap of drops before coalescing is a consequence of earlier coalescing events and drop growth. A deviation of ca. 0.15 is reported on a RP confirming the impossibility for new merged drops to maintain their spherical shape throughout multiple coalescing events. On the other hand, on a LL the degree of sphericity for both coalescing and new merged drops is maintained fairly constant and above 0.97 throughout growth and multiple coalescing events independently of the drop size interval. The maximum sphericity difference for a LL is estimated as 0.03, which is at least one order of magnitude smaller than that of a RP, suggesting the lower adhesion between condensing drops and a LL when compared to a RP. When looking into the PDMS counterparts, the sphericity of new merged drops is considerably lower than for a LL. Sphericity values ca. 0.9 are reported on coated samples, which also evidence the greater

adhesion of the triple contact line on the counterpart samples when compared to non-coated LL. The ability for a LL surface to sustain spherical drops throughout condensation, infers the lower adhesion of the condensate to a LL when compared to RP, RP_{PDMS} and LL_{PDMS} surfaces, which is further demonstrated by a surface energy analysis presented next.

Surface Energy Analysis

From optical microscopy experimental observations of the dynamics of condensation and coalescence presented in Figure 3 and Figure 4, and the quantification of the drop shape included in Figure 5, the different interactions between the condensate and the various surfaces studied are evident. Next, we focus our attention on the effect of each surface on the coalescence performance paying special attention to the roughness tier and to the accepted and observed wetting behaviours. On a rose petal, drops typically wet the micro-structures (Figure 6a) inducing a sticky non-wetting behaviour,[44, 51, 55] whereas on a lotus leaf, drops rest above the micro- and the nano-structures in a Cassie stable state (Figure 6b) prompting a super-repellent non-wetting behaviour.[44, 52, 55] Schematics (top row) and representative optical microscopy snapshots (bottom row) before and after drop coalescence on a metallic RP and on a metallic LL are presented in Figure 6a and Figure 6b, respectively.

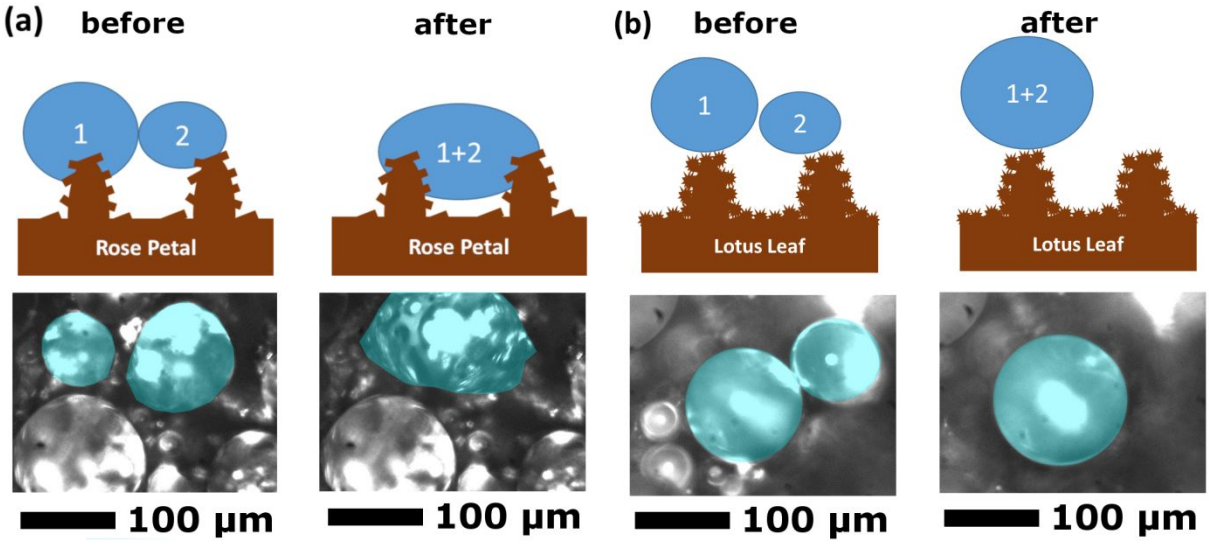

Figure 6 - (Top) Schematics of (a) the sticky non-wetting behavior on a metallic RP and (b) the super-repellent non-wetting behavior on a metallic LL surfaces (left) before and (right) after coalescence.[51-52] (bottom) Representative optical microscopy snapshots of coalescence on (a) a metallic RP and (b) a metallic LL surfaces at ca. 7 minutes taken from Figure 4. Time between snapshots is 0.48 seconds. Scale bars are 100 µm.

To differentiate the various nature of the condensate-surface interactions, next, we conduct a surface energy analysis to elucidate the different wetting and coalescing behaviors reported, which in turn will dictate the final condensation mechanism as either filmwise or dropwise. Surface energy analysis is based on the different tiers of roughness, *i.e.*, different multi-scale tiers of surface structure underneath the condensing drops, as well as on the accepted sticky and super-repellent non-wetting behaviors earlier proposed for a rose petal and for a lotus leaf, respectively. Sticky and super-repellent non-wetting behaviors were further confirmed by macroscopic contact angle measurements reported in Table 1.[44, 52, 56] Sticky non-wetting behavior is typically characterized by high advancing contact angle with contact angle hysteresis in the order of 10^0 to 100^0, whereas the super-repellent non-wetting behavior offers high advancing contact angle with relatively low contact angle hysteresis $<10^0$.

We then estimate the ratio of surface energy of adhesion (E_{adh}) over the total excess of surface energy ($E_{ex\text{-}surf}$) as: E_{adh} / $E_{ex\text{-}surf}$. E_{adh} / $E_{ex\text{-}surf}$ evaluates the amount of excess of surface free energy required to overcome the energy of adhesion for the detachment of the triple contact line upon drop growth, coalescence and/or by gravity depending on the surface studied.[57, 59]

Before going into the details of the surface energy analysis proposed, we ease the reader by introducing the basic equations for the calculations of the energy of adhesion E_{adh} and the total excess of surface energy $E_{ex\text{-}surf}$. On one hand, on an ideal flat hydrophobic surface, the surface adhesion energy per unit of area E_{adh} is estimated by making use of the Young-Dupré's equation, which in turn indicates the energy of adhesion between the dry state (a surface and a drop not in contact) and the final state (drop resting on the solid surface) as[60-61]:

$$E_{\text{adh,flat}} = \gamma_{\text{lg}}(1 + \cos\theta_e)A \quad (1)$$

where γ_{lg} is the surface tensions liquid-gas, θ_e is the intrinsic equilibrium contact angle and A solid-liquid interfacial wetted area equals πR_b^2 with R_b as the drop wetting base radius. On the other hand, the total excess of surface energy on an ideal flat hydrophobic surface $E_{ex\text{-}surf,flat}$ is obtained by estimating the Gibbs free energy of a drop sitting on a solid surface as[62-63]:

$$E_{\text{ex}-\text{surf,flat}} = \gamma_{\text{lg}}S + (\gamma_{\text{sl}} - \gamma_{\text{sg}})A \quad (2)$$

where γ_{sl} and γ_{sg} are the surface tensions solid-liquid and solid-gas, respectively, and S is the drop surface area approximated to a spherical cap and equals $2\pi Rh$, with h as the height of the drop $h = R(1 - \cos\theta_e)$, and R as the radius of the drop which can be extracted from top view.

Next, due to the different surface structure underneath the condensing drops and to the different wetting behavior, we now differentiate and estimate the ratio of surface energy of adhesion over the total excess of surface energy E_{adh} / $E_{ex\text{-}surf}$ depending on the surface studied:

Rose Petal: On a metallic rose petal, the bottom of the drop will deform wetting the Tier 2 micro-structures decorating the main Tier 1, as in the Wenzel "sticky" mode or partial wetting regime.[55, 64-65] As the condensate wets the stacked "Lego bricks", *i.e.*, the Tier 2 micro-structures, the solid-liquid interface area effectively increases and so does the condensate energy of adhesion to the surface following the Wenzel roughness factor r.[64] By introducing the rose petal roughness factor r_{RP} in Equation 1, the energy of adhesion of a metallic RP $E_{adh,RP}$ for a partially wetting drop in the Wenzel regime,[55-56] is calculated as Equation 3:[66-67]

$$E_{adh,RP} = \pi r_{RP}\gamma_{lg}(1 + \cos\theta_i)R_b^2 \quad (3)$$

where, θ_i is the intrinsic advancing contact angle on the smooth metallic surface, and R_b is equals $\sin\theta_a R$ where θ_a is the macroscopic advancing contact angle reported in Table 1. On one hand, the roughness factor r_{RP} accounts for the increase on the effective solid-liquid interfacial area due to the partial deformation below the drop as the drop wets the micro-structures in the Wenzel state, *i.e.*, $r \sim r_{RP} > 1$.[64] r_{RP} incurred by Tier 1 can be estimated as $r_{RP\_TIER1} = 1 + h\sum_{i=1}^{N} l_{c,i}/A$, where h and $l_{c,i}$ are the height and the characteristic length of the micro-structures, respectively, and A is the total surface area. The height h is obtained from 3D optical laser scanning microscopy as *ca.* 241 ± 27 μm (see 3D optical laser scanning microscopy snapshots from a metallic rose petal in the accompanying Supporting Information S3, Figure S1), while $l_{c,i}$ and A are measured from SEM images (Figure 1). By assuming the micro-structures as squared pillars, $l_{c,i}$ can be approximated as $l_{c,i} = A_{pillar,i}^{0.5}$, where $A_{pillar,i}$ is the 2D top area for each of the structures. $A_{pillar,i}$ was averaged from 10 independent micro-structures. The roughness value of the Tier 1 r_{RP_TIER1} is then estimated as 2.9. Measured h and $l_{c,i}$ values for Tier 1 are in agreement with those previously reported in the work of Frankiewicz and Attinger[44] for a wetting-like RP surface fabricated following the same etching procedure. Further, the stacked "Lego bricks" forming the Tier 2 also incur in the increase in the roughness factor. To assess the increment of surface roughness induced by the Tier 2, we estimate the

average surface roughness from the top of Tier 1 micro-structures by making use of 3D optical laser scanning microscopy focusing at the micro-structure tops (see Figure S2, Figure S3 and Figure S4 in the accompanying Supporting Information). The average surface roughness S_a was estimated from 3D optical laser scanning microscopy and averaged for 3 independent areas. Then, the roughness factor due to the Tier 2 micro- structures r_{RP_TIER2} can be estimated as 1.6 ± 0.6, and must be accounted for. By making use of a representative generic multi-scale model, the roughness factor accounting for both Tier 1 and Tier 2 is then estimated as: $r_{RP} \sim r_{RP\_TIER1} * r_{RP\_TIER2} \sim 4.6$.[44] On other hand, the intrinsic advancing contact angle θ_i for a water drop on a smooth copper surface after ambient exposure $\theta_{i,Cu}$ was measured as 94° ± 2°. We note here that due upon ambient exposure, $\theta_{i,Cu}$ may be greater than that on a smooth cleaned copper surface θ_{Cu}.[37, 48]

To be able to account for the different surface structure and wetting behaviour, the excess of surface energy for a spherical drop on a metallic RP surface $E_{ex\text{-}surf,RP}$ is, on the other hand calculated by subtracting the energy of adhesion $E_{adh\text{-}RP}$ from the total surface energy of the drop $E_{surf,RP}$ as: $E_{ex-surf,RP} = (E_{surf,RP} - E_{adh,RP})$. The total surface energy of the drop on a RP surface, $E_{surf,RP}$, is estimated from the expression proposed in the work of Chen *et al*. and Zhang *et al.* for a spherical drop in the composite state:[57, 67-68]

$$E_{surf,RP} = \pi\left[\left(\frac{2}{(1+\cos\theta_a)} - 2f_n r_{RP} + r_{RP}(1 - f_n cos\theta_{i,Cu})\right)\gamma_{lg} + r_{RP} r_n \gamma_{sg}\right] R_b^2 \quad (4)$$

where f_n and r_n are the solid fraction and the roughness of the nanostructures, respectively. On a RP, due to the absence of nano-scale features, it is safe to assume $f_n = 0$ and $r_n = 1$. Moreover, since complete wetting of the micro-structures occurs, the right hand side of Equation 4 accounting for the solid-gas interfacial energy below the drop $\sim r_{RP} r_n \gamma_{sg}$ can be neglected.[55]

Lotus Leaf: On a metallic lotus leaf, a drop will rest/condense in the Cassie stable state or suspended above the micro- and the nano-structures as in the non-wetting regime.[56, 65, 69] Then, the energy of adhesion of a drop sitting/condensing on a LL $E_{adh,LL}$ is calculated by introducing the solid fraction f_{LL} underneath the condensing drops in Equation 1 as:[57, 66-67]

$$E_{adh,LL} = \pi f_{LL} \gamma_{lg} (1 + \cos\theta_i) R_b^2 \quad (5)$$

In this case, due to the additional oxidation step, θ_i must be considered as the advancing contact angle on a thin copper oxide film surface $\theta_{i,CuO}$ rather than on flat copper surface $\theta_{i,Cu}$ as per the RP case. Hence, here we adopt θ_i as the advancing contact angle on a thin copper film

surface after ambient exposure (further change in composition due to physical absorption of oxygen and/or that of VOCs at the interface) as in the work of Chang *et al.* $\theta_{i,CuO} = 110°$.[37, 48] The solid fraction on a LL surface without nano-structures can be estimated from the SEM experimental observations of the micro-structures tops and equals 0.45 ± 0.07. Due to the copper oxide nano-structures decorating the micro-structure tops, the expected solid fraction on a LL shall be lower than the one earlier reported. In order to provide a more accurate estimation of the solid fraction, we make use of the Cassie-Baxter equation as: $f_{LL} = \frac{\cos\theta_a + 1}{\cos\theta_i + 1} = 0.229$.[69-70] It is worth noting that the surface roughness in the presence of nano-structures can be estimated from the following equation $r = 1 + {}^{\pi d_n h_n}/_{l_n^2}$, where d_n, h_n and l_n are the diameter, height and spacing of the nano-structures, which can be extracted from SEM snapshots from Figure 1 and Figure S10 in the accompanying Supporting Information. Nonetheless, in the present case, the micro-structure roughness and the solid fraction provide a more relevant characterization in terms of the estimated solid-condensate interactions and the proposed surface energy analysis.

The excess of surface energy for a spherical drop on a LL $E_{ex\text{-}surf,LL}$ is also calculated by subtracting the energy of adhesion $E_{adh,LL}$ from the total surface energy of the drop $E_{surf,LL}$: $E_{ex-surf,LL} = (E_{surf,LL} - E_{adh,LL})$. The total surface energy of the drop on a LL $E_{surf,LL}$ is estimated as for a drop in the suspended state in the presence of micro- and nano-structures:[57, 67]

$$E_{surf,LL} = \pi\left[\left(\frac{2}{(1+\cos\theta_a)} + 1 - f_{LL}\right)\gamma_{lg} + f_{LL}(\gamma_{sg} - \gamma_{lg}cos\theta_i) + \gamma_{sg}(r - f_{LL})\right]R_b^2 \quad (6)$$

where r accounts for the increase in interfacial area solid-gas due to presence of micro-structures when compared to the flat sample. Since micro-structures were fabricated following the very same etching procedure, *i.e.*, same temperature, time and composition of the etching solution as for RP, r in Equation 6 can be approximated to that of r_{RP}.[44]

Equations 3 to 6 are function of the drop base radius R_b though. In order to offer a more appropriate comparison between drops of the same size, *i.e.*, same drop radius and volume, we substitute $R_b = \sin\theta_a R$. It is noteworthy that for the same drop radius R, due to the different macroscopic advancing contact angles, the deviation in volume when comparing a drop on a LL to that on a RP is within 3%. Next, $E_{adh,RP}$, $E_{adh,LL}$, $E_{surf.RP}$ and $E_{surf,LL,}$ function of the drop

radius R for both RP and LL are reported in Table 2. In addition, the ratio E_{adh} / $E_{ex\text{-}surf}$ is included in Table 2:

Table 2 – Summary of the energy of adhesion E_{adh}, surface energy E_{surf} and excess of surface energy $E_{ex\text{-}surf}$, of a drop function of drop radius R, and ratio E_{adh} / $E_{ex\text{-}surf}$ for a metallic RP and for a metallic LL surfaces.

Energy / Type of Surface	Rose Petal (RP)	Lotus Leaf (LL)
E_{adh} (N)	0.27 R^2	0.015 R^2
E_{surf} (N)	1.15 R^2	1.005 R^2
$E_{ex\text{-}surf}$ (N)	0.862 R^2	0.985 R^2
E_{adh} / $E_{ex\text{-}surf}$	0.31	0.015

From Table 2, when comparing similar drop volumes, *ca*. 18 times greater E_{adh} is reported on a RP when compared to a LL. Differences on E_{adh} arise mainly from the dissimilar drop wetting behaviours induced by the different surface structure underneath the condensing drops. The ratio of energy of adhesion to total excess of surface energy E_{adh} / $E_{ex\text{-}surf}$ of a drop on a RP is 0.31 compared to 0.015 on a LL. At least one order of magnitude greater fraction of the $E_{ex\text{-}surf}$ must be utilized to overcome the E_{adh} in the case of a partially wetting drop on a RP when compared to a suspended one on a LL. Such ratio is in agreement with the sphericity difference quantified and reported in Figure 5 when comparing a LL and a RP.

The above energy analysis demonstrates the lower excess of free energy required to overcome the adhesion for suspended drops in the presence of a nano-scale roughness (Tier 3) prompting a Cassie stable state on a LL, when compared to absence of nano-scale roughness inducing a Wenzel wetting state on a RP. The rather low $E_{adh,LL}$ reported on a LL, evidences the easiness for the triple phase contact line to depin upon coalescence, hence the spherical shape adopted by new merged drops throughout condensation (see LL on Figure 3, Figure 4, Figure 5 and Figure 6). The rather low $E_{adh,LL}$ on a LL is expected to eventually prompt the shedding of the condensate from the surface by gravity in a dropwise condensation fashion.

Furthermore, to demonstrate the greater adhesion of drops condensing on a RP when compared to a LL, a more simplified energy of adhesion analysis taking into account solely the

interactions at the solid-liquid interface, can be estimated as the ratio $E_{\mathrm{adh,RP}}$ (Eq. 3) to $E_{\mathrm{adh,LL}}$ (Eq. 5):

$$\frac{E_{\mathrm{adh,RP}}}{E_{\mathrm{adh,LL}}} = \frac{\pi r_{\mathrm{RP}} \gamma_{\mathrm{lg}} (1 + cos\theta_{\mathrm{i,Cu}}) R_{\mathrm{b}}^2}{\pi f_{\mathrm{LL}} \gamma_{\mathrm{lg}} (1 + cos\theta_{\mathrm{i,CuO}}) R_{\mathrm{b}}^2} \quad (7)$$

For the same drop base radius R_{b}, the ratio $E_{\mathrm{adh,RP}}/E_{\mathrm{adh,LL}}$ can be reduced to $\sim \frac{r_{RP}(1+\cos\theta_{\mathrm{i,Cu}})}{f_{\mathrm{LL}}(1+\cos\theta_{\mathrm{i,CuO}})}$ equals *ca.* 28. This value is at least one order of magnitude greater for a RP than for a LL, which is in agreement with the ratio $(E_{\mathrm{adh}} / E_{\mathrm{ex\text{-}surf}})_{\mathrm{RP}}$ to $(E_{\mathrm{adh}} / E_{\mathrm{ex\text{-}surf}})_{\mathrm{LL}}$ *ca.* 20.6. The greater energy of adhesion to excess of free energy on a RP inducing greater adhesion/"stickiness" when compared to a LL is then demonstrated.

The energy analysis presented above is in excellent agreement with optical microscopy observations of drop growth and coalescence during the dynamics of condensation presented in Figure 3, Figure 4 and Figure 6, with the drop sphericity quantification presented in Figure 4, as well as with macroscopic contact angle hysteresis measurements presented in Table 1. The low $E_{\mathrm{adh,LL}}$ as well as the low $E_{\mathrm{adh,LL}} / E_{\mathrm{ex\text{-}surf,LL}}$ reported on a metallic LL supports the low contact angle hysteresis from Table 1 and the depinning of the triple phase contact line upon coalescence and during drop growth. Hence the occurrence of spherical drops throughout the entire duration of the experimental observations. Conversely on a RP, the high $E_{\mathrm{adh,RP}}$ and $E_{\mathrm{adh,RP}} / E_{\mathrm{ex\text{-}surf,RP}}$ induce the greater pinning of the contact line and the formation of non-spherical drops with high adhesion.

PDMS counterparts: It is worth noting that the same energy analysis presented above can be readily applied to the PDMS counterparts. Based on the high contact angle hysteresis reported in Table 1, as well as the occurrence of drops rather than spherical throghout condensation and coalescence, it is safe to assume that on both PDMS coated surfaces, drops grow in the partially wetting regime. Here the drop interface deforms closely following the shape of the micro-structures, *i.e.*, the stacked "Lego bricks", as in the case of a RP. Then, for $\mathrm{RP_{PDMS}}$ counterparts, $r_{\mathrm{RP\text{-}PDMS}}$ can be approximated to r_{RP}. In the case of a $\mathrm{LL_{PDMS}}$, since the condensate wets the nanofibrils, $r_{\mathrm{LL\text{-}PDMS}}$ can be approximated as f_{LL}. We stress here that the PDMS slightly changes the surface structure/roughness of the $\mathrm{RP_{PDMS}}$ and $\mathrm{LL_{PDMS}}$ counter-parts as evidenced from SEM presented in Figure 1. Nonetheless, the presence of PDMS nano-globules may increase the $r_{\mathrm{RP\text{-}PDMS}}$ when compared to r_{RP}, while the smoothening of the nano-structures in the case of a $\mathrm{LL_{PDMS}}$ may increase the solid fraction $f_{\mathrm{LL\text{-}PDMS}}$ when compared f_{LL}. In either case, the presence of the PDMS yields greater $E_{\mathrm{adh,RP\text{-}PDMS}}$ and $E_{\mathrm{adh,LL\text{-}PDMS}}$ and still provides one order

of magnitude greater adhesion than $E_{adh,LL}$. The intrinsic advancing contact angle for a drop on a flat smooth PDMS surface is measured as $\theta_{i,PDMS} = 115° \pm 3°$. Then, by substituting $r_{RP\text{-}PDMS}$, $r_{LL\text{-}PDMS}$ and $\theta_{i,PDMS}$ in Equation 3, $E_{adh,RP\text{-}PDMS}$ and $E_{adh,LL\text{-}PDMS}$ function of the drop base radius R_b are estimated as ~ 0.09 R^2 N and 0.17 R^2 N, respectively. $E_{adh,RP\text{-}PDMS}$ and $E_{adh,LL\text{-}PDMS}$ are found to be in the same order of magnitude as $E_{adh,RP}$ and one order of magnitude greater than $E_{adh,LL}$, which also evidences the greater nature of the adhesion of the PDMS counterparts. We note here that the PDMS slightly changes the surface structure/roughness of the RP_{PDMS} and LL_{PDMS} counter-parts as evidenced from SEM presented in Figure 1. Nonetheless, the presence of PDMS nano-globules may increase the $r_{RP\text{-}PDMS}$ when compared to r_{RP}, while the smoothening of the nano-structures in the case of a LL_{PDMS} may increase the solid fraction $f_{LL\text{-}PDMS}$ when compared f_{LL}. In either case, the presence of the PDMS yields greater $E_{adh,RP\text{-}PDMS}$ and $E_{adh,LL\text{-}PDMS}$ and still provides one order of magnitude greater adhesion than $E_{adh,LL}$.

The low drop adhesion and the occurrence of spherical drops throughout coalescence and growth reported on a LL when compared to the other three samples (RP, RP_{PDMS} and LL_{PDMS}) is then demonstrated by optical microscopy experimental observations, macroscopic contact angle measurements and by our drop surface energy analysis. Next to confirm the expected different condensation behaviours depending on the surface studied, experimental observations of condensation at the macroscale are presented.

Experimental Observations at the Macroscale

From the energy analysis proposed above we may stipulate that the rather low adhesion of the condensate to the super-repellent LL surface should lead to continuous shedding of drops with sizes in the order of millimetres in a sustained dropwise condensation manner.[7, 71] Whereas on sticky RP, RP_{PDMS} and LL_{PDMS} surfaces, because of the greater adhesion of the condensate wetting the different tiers of roughness, the depinning of the triple phase contact line does not ensue upon drop coalescence and/or during drop growth. Hence, as condensation develops, filmwise condensation is expected. In order to verify the above expected condensation mechanisms, we assess the condensation behaviour at the macroscale on all four samples. condensation conditions as included within the Materials and Methods Section were as follows: ambient temperature T_{amb} = 30 ± 2 °C and relative humidity RH = 80 ± 5% with a surface temperature T_{wall} =10 ± 1 °C, providing a degree of supersaturation approximately 2.78. Figure

7 shows characteristic macroscopic snapshots during condensation on a metallic RP, on a RP_{PDMS}, on a metallic LL and on a LL_{PDMS}. Red circles are included to readily identify the shape of the condensing drops. To preserve the non-wetting characteristics of the surfaces as per received, we stress here that prior to experimental observations surfaces were only rinsed with deionized water and dried with filtered air.[44, 48-49]

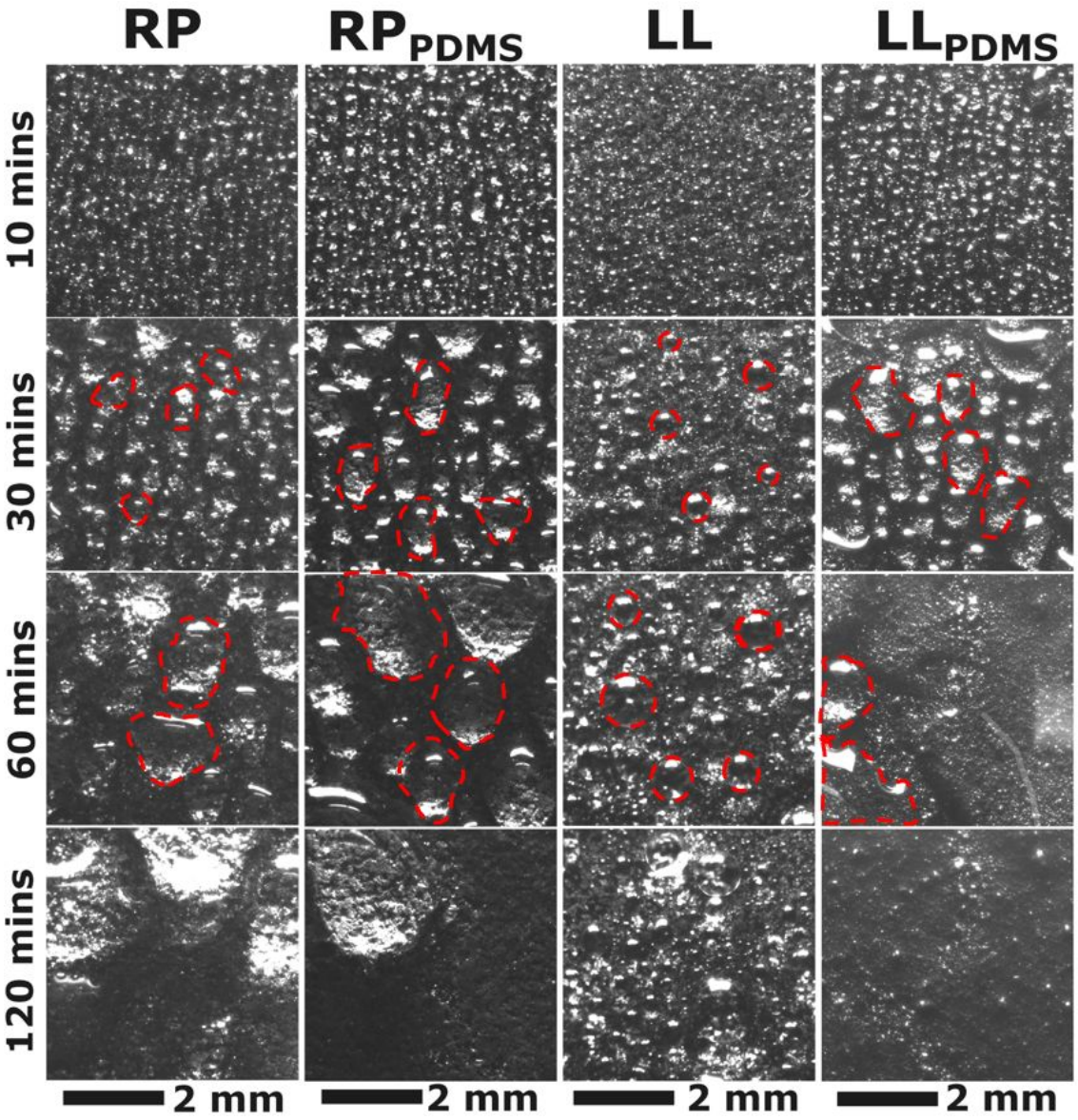

Figure 7 - Representative characteristic macroscopic snapshots of condensation behavior on a metallic RP, a coated RP_{PDMS}, a metallic LL, and a coated LL_{PDMS} surfaces at t = 10, 30, 60 and 120 minutes with t = 0 minutes as the onset of condensation. Complete macroscopic experimental observations can be found in the accompanying Supporting Information as Video S5 for a metallic RP, Video S6 for a RP_{PDMS}, Video S7 for a metallic LL and Video S8 for a LL_{PDMS}. The contour of non-spherical drops on RP, RP_{PDMS} and RP_{PDMS} and spherical ones on LL are highlighted in dashed red lines for easier comparison. Scale bar is 2 mm.

Macroscopic snapshots presented in Figure 7 at 10 minutes are consistent with optical microscopy observations depicted in Figure 3. Drops in the order of hundreds of μm can be discerned on all four surfaces. As condensation develops, for 30 and 60 minutes, on one hand drops with irregular shapes other than spherical become evident on RP, RP_{PDMS} and LL_{PDMS}, whereas on a LL on the other hand, the spherical nature of the drops is sustained throughout the entire duration of the condensation experimental observations. On a metallic LL, the uniform drop size distribution and the absence of drops with sizes above few millimetres at different condensation times, evidences the self-detachment nature of the condensate and the condensation performance in a sustained dropwise fashion throughout the entire duration of the experimental observations (see Supporting Information, Video S7).[7, 72-73] Despites the rather high degree of supersaturation reported, dropwise condensation ensues on our metallic LL surface. On the contrary, on a RP, a RP_{PDMS} and a LL_{PDMS}, condensation behaviour transitioned from dropwise to filmwise condensation (see Supporting Information, Video S5, Video S6 and Video S8). The next figure, Figure 8, demonstrates the transition from dropwise to complete filmwise condensation occurring on a RP, a RP_{PDMS} and a LL_{PDMS} surfaces, and a characteristic drop shedding event on a LL at *ca.* 120 minutes. Transition to filmwise is characterized by the coalescence of several irregular drops with sizes above few millimetres into a film.

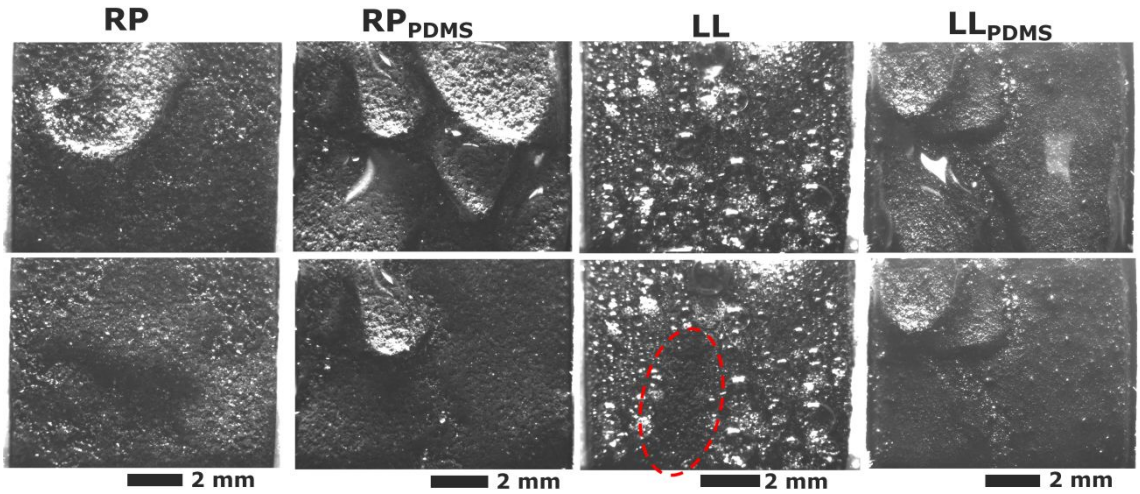

Figure 8 - Characteristic macroscopic snapshots of the transition from dropwise to filmwise condensation on a metallic RP, a coated RP_{PDMS}, and a coated LL_{PDMS} and characteristic drop shedding event on a metallic LL at *t* ca. 120 minutes. Time between frames is 1 second. Dashed circle shows refreshed area for drop re-nucleation and growth. Scale bar is 2 mm.

On one hand, from Figure 8, on RP, a RP_{PDMS} and a LL_{PDMS} the complete transition to filmwise condensation where the surfaces are completely covered with the condensate after *ca.* 2 hours, reveals that filmwise is the final steady state condensation behaviour. On the other hand, on a LL the continuous nucleation, growth, coalescence and shedding of drops in a dropwise condensation manner is reported.

Last, from macroscopic experimental observations, quantification on the surface area covered by the condensate and the drop density along with the average drop size at different condensation times are presented in Figure 9a and Figure 9b, respectively:

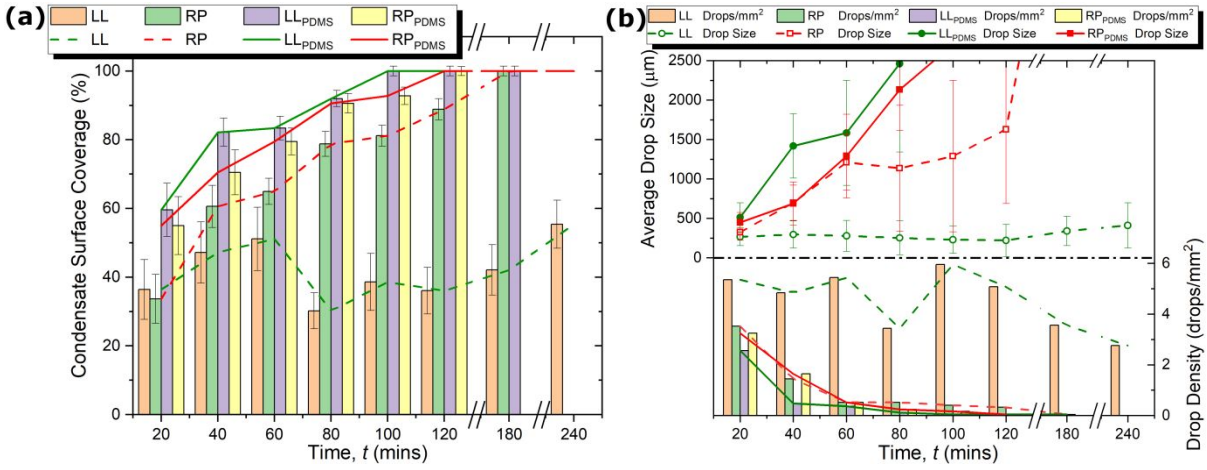

Figure 9 – Quantification of (a) surface coverage (%) versus time and (b) average drop size equivalent diameter (µm) and drop density (drops/mm^2) for LL, RP, RP_{PDMS}, and LL_{PDMS}. Dashed lines for (green) LL and (red) RP and solid lines for (red) RP_{PDMS} and (green) LL_{PDMS} are included to illustrate the trend.

Figure 9a shows the continuous increase in the area covered by the condensate, which eventually develops into filmwise condensation on RP, RP_{PDMS} and LL_{PDMS} as earlier introduce in Figure 7. The increase in surface area covered by the condensate on RP, RP_{PDMS} and LL_{PDMS} is supported by the decrease in the drop density and the increase in the average drop size as condensation time ensues as presented in Figure 9b. As the condensate undergoes drop growth and different coalescing events, the high adhesion exerted by a RP, a RP_{PDMS} and a LL_{PDMS} does not allow for the contact line depinning and/or the shedding of the condensate, which is supported by earlier micro- and macro-scopic experimental observations from Figure 4 and Figure 7, respectively. On the other hand, on a LL the surface area covered by the condensate (Figure 9a) oscillates between 35% and 60% demonstrating the occurrence of shedding events

during condensation as shown in Figure 8. Moreover, Figure 9b shows that the average drop size equivalent diameter (estimated as $D_{eq} = \sqrt{4A_{drop}/\pi}$ with A_{drop} as the drop surface coverage area extracted from macroscopic experimental observations) is also maintain below 500 microns and that the drop density also fluctuates as a consequence of drop shedding, which refreshes the area for drop renucleation and growth in a dropwise condensation fashion.

Although the intrinsic wettability of the PDMS coupled with surface structure of the coated counter-parts RP_{PDMS} and a LL_{PDMS} surfaces should lead to non-wetting and dropwise condensation behavior, the smoothening of the Tier 3 fibrils tops in the case of a LL_{PDMS} is put forward as the plausible mechanism for the different coalescence and final condensation mechanisms reported. The chemistry of the nano-structures as well as the geometry of the copper oxide nano-structures along with the chemistry and the geometry of the globular PDMS agglomerates plays a crucial role on the dynamics and on the final condensation behavior and is suggested for future studies on wettability and on condensation phase-change. Moreover, further considerations on the mechanical robustness of the surfaces are discussed next. Fabricated metallic RP and LL surfaces do not delaminate opposite to polymer coated ones, which are prone to delaminate as a consequence of the weak bonding between the metal and/or the metal oxide and the polymeric coating. In addition, RP and LL surfaces presented here are more ductile (less brittle) than silicon as per the ability to withstand critical heat flux (CHF) without properties degradation.[74] Last, upon surface mechanical abrasion, such as sand-blasting, the micro-structure tops act as sacrificial elements protecting the nano-structured copper oxide in between the structures maintaining similar advancing contact angles to those on the original surface.[10] It is worth noting here that although the non-wetting behavior can be maintained after mechanical abrasion, the straight pillared nature of the micro-structures coupled with the removal of the copper oxide nano-structures from the micro-structure tops might lead to a different final condensation behavior similar to the one reported on a RP. Further studies will focus on the robustness of such surfaces.

The presence of copper oxide nano-structures coupled with ambient exposure provide the lotus leaf surfaces with their intrinsic super-repellent non-wetting behaviour. Then, the continuous dropwise condensation behaviour on a LL is further demonstrated by macro- and microscopic experimental observations and quantification of the drop sphericity and of the condensate surface coverage, as well as by the proposed energy analysis.[57, 59] The first biomimetic lotus leaf surface engineered from a purely metallic material without the assistance of a polymeric hydrophobic coating able to perform in a continuous dropwise condensation is here reported.

The work introduced here opens a new avenue for the design and fabrication of non-coated metallic surfaces with excellent shedding performance, which are paramount for applications such as anti-icing, anti-fogging and condensation, amongst others.

CONCLUSIONS

The wetting behaviour and the condensation performance on two non-wetting surfaces engineered from copper without the assistance of a conformal hydrophobic polymer was investigated. On one hand, on a metallic surface comprising two micro-scopic tiers of roughness, which wetting behaviour resembles the sticky non-wetting behaviour of a rose petal, the final condensation behaviour is that of filmwise. Whereas, on the other hand, on a metallic lotus leaf, the additional oxide third nano-scale tier prompts the super-repellent non-wetting behaviour and the continuous condensation performance in a dropwise fashion. A drop surface energy analysis based on the two accepted macroscopic wetting behaviours *i.e.*, sticky non-wetting versus super-repellent non-wetting, and on the different tiers of roughness, demonstrates the greater adhesion of drops condensing on a metallic rose petal when compared to a metallic lotus leaf. As a consequence of the rather low drop adhesion of the condensate to the metallic lotus leaf, drops are able to maintain their spherical shape during growth and coalescence and are able to detach from the surface by gravity. In addition, the wetting to non-wetting transition on the rose petal and lotus leaf surfaces upon ambient exposure inducing the reported dropwise condensation behaviour on a lotus leaf is here demonstrated. Further, PDMS coated metallic rose petal and PDMS coated metallic lotus leaf counterparts were also investigated. The wetting behaviour and the final condensation behaviour reported on both PDMS coated surfaces was that of sticky non-wetting and filmwise, respectively. The superior performance of our metallic engineered copper lotus leaf surface able to sustain continuous dropwise condensation is owed to the presence of a third nano-scale roughness tier fabricated by common oxidation procedures and subjected to ambient exposure when compared to a solely micro-structured engineered copper rose petal. We conclude on the occurrence of continuous dropwise condensation on a hierarchical bioinspired engineered metallic surface without the assistance of a conformal polymeric hydrophobic coating, which is of paramount interest for applications where the stability and the durability of the coating are an issue.

MATERIALS AND METHODS

Sample Fabrication

A metallic lotus leaf (LL) and a metallic rose petal (RP) surface were fabricated following the same etching and oxidation procedures reported in the work of Frankiewicz and Attinger.[44] Copper blocks of 9 x 9 x 3 mm^3 were firstly sanded and then rinsed with isopropanol to remove the native oxide layer. Thereafter, samples were sonicated in a 5% w/w hydrochloric acid-water (HCl-H_2O) solution for 15 minutes and then immersed in deionized water for further 10 minutes. Both RP and LL samples were fabricated by etching previously cleaned copper samples with a solution of iron chloride ($FeCl_3$) and HCl at ambient temperature for 36 hours. The $FeCl_3$ reacts with the copper, whereas the HCl reduces the etching rate.[44] Moreover, LL samples were fabricated by subjecting etched samples to an additional oxidation step. Oxidation was carried out with ammonium hydroxide (NH_4OH) at 65 °C for 48 hours.[75] After fabrication and before experimental observations, all samples were further sonicated in deionized water for 15 minutes and finally dried with compressed air to remove any contaminants. In addition, RP_{PDMS} and LL_{PDMS} counterparts were prepared by vapour deposition of polydimethylsiloxane (PDMS).[53]

Surface Characterization

The surface structure of a LL, a RP and their PDMS counterparts was assessed in an Environmental Scanning Electron Microscope (ESEM, Versa 3D, FEI Co., USA). Whereas the micro-structures height, h, was measured in a 3D Optical Laser Scanning Microscope (OLS4000, Olympus, Tokyo, Japan). In addition, to confirm the different non-wetting behaviours earlier reported in literature as sticky non-wetting on a RP and super-repellent non-wetting on a LL, equilibrium contact angle, θ_0 (deg), advancing contact angle, θ_a (deg), receding contact angle, θ_r (deg), and contact angle hysteresis, CAH = θ_a - θ_r (deg), were assessed in a custom-built contact angle goniometer. The maximum standard deviation observed in contact angle measurements was 3°.

Prior to addressing the wetting to non-wetting transition upon ambient exposure on a RP and on a LL, surfaces were subjected to oxygen plasma cleaning in a plasma etching system FA-1 from SAMCO (Japan) under 55 W power and oxygen flow of 10 mL min^{-1} for 3 minutes. Thereafter surfaces were subjected to contact angle, Energy Dispersive X-Ray Spectroscopy (EDS) measurements to address the wetting and the surface chemistry characterization at different exposure times.

After oxygen plasma cleaning, the advancing contact angle, θ_a (deg), was measured in a custom-built contact angle goniometer. Average advancing contact angle, θ_a (deg), and standard deviation of at least three independent measurements are included in Table S1 in the accompanying Supporting Information.

Energy Dispersive X-Ray Spectroscopy (EDS) was carried out in a Field Emission SEM JSM-7900F from JEOL (Tokyo, Japan) at different exposure times. The main elements analysed were Carbon, Oxygen and Copper, which accounted for more than 96% of the elements present at the surface and the chemical composition was analysed at 0 hours, 4 hours, 16 hours, 36 hours and 108 hours after oxygen plasma cleaning procedure. Quantification on the chemical species present at the surface of a RP and of a LL at different exposure times are included in Table S2 and Table S3, respectively, in Section S6 in the accompanying Supporting Information.

Condensation Experimental Observations

Optical microscopy and macroscopic condensation experimental observations were conducted using a PR-3KT environmental chamber from ESPEC Corp. (Japan). Ambient temperature and relative humidity were set as $T_{amb} = 30 \pm 2$ °C and $RH = 80 \pm 5\%$. Deviations reported for both T_{amb} and RH were the maximum deviations observed during the complete duration of each of the experimental observations. A custom-built water-cooled Peltier stage was used to induce condensation phase change. Samples were embedded on a PTFE block to ensure unidirectional heat transfer between the Peltier stage and the test sample. Each sample was then affixed with double side copper tape on the copper block and Peltier stage was finally placed vertically inside the chamber. The temperature of the Peltier stage T_{wall} was controlled with a PID at 10 ± 1 °C. The degree of supersaturation S estimated as the ratio of the water vapour pressure at the chamber environmental conditions P_v to the water vapour saturation pressure at the surface/Peltier stage temperature P_{wall} equals $S = P_v / P_{wall} = 2.78 \pm 0.5$. Condensation dynamics at the micro-scale were recorded using a high-resolution optical microscopy zoom lens from Keyence (VH-Z500R) attached to a CCD camera Sentech STC-MC152USB placed perpendicular to the surface. Magnification was set at 500x providing a field-of-view of 610 x 457 μm^2. Whereas observations at the macroscale were carried out using a Cosmicar TV zoom lens with a 40 mm spacing ring. Any image processing and analysis was conducted with ImageJ.[58]

ASSOCIATED CONTENT

Supporting Information

The Supporting Information is available free of charge on the ACS Publications website at DOI: XX.XXXXX/acsami.XXXXXXX.

Additional description of the optical microscopy videos S1, S2, S3 and S4 (Section S1), macroscopic videos S5, S6, S7 and S8 (Section S2), 3D Optical Laser Scanning Microscopy on the metallic rose petal (Section S3), 3D Optical Laser Scanning Microscopy on the metallic lotus leaf (Section S4), estimation of the solid fraction on the metallic lotus leaf surface (Section S4), advancing contact angle measurements function of exposure time for a RP and a LL (Section S5), and quantification of the surface chemical composition at different exposure times for a RP and a LL via Energy Dispersive X-Ray Spectroscopy (EDS) (Section S6) (PDF)

Video S1: Optical Microscopy video of the dynamics of condensation phase change on a metallic rose petal RP (AVI)

Video S2: Optical Microscopy video of the dynamics of condensation phase change on a metallic rose petal coated with polydimethylsiloxane (PDMS) RP_{PDMS} (AVI)

Video S3. Optical Microscopy video of the dynamics of condensation phase change on a metallic lotus leaf LL (AVI)

Video S4. Optical Microscopy video of the dynamics of condensation phase change on a metallic lotus leaf coated with polydimethylsiloxane (PDMS) LL_{PDMS} (AVI)

Video S5. Macroscopic video of the dynamics of condensation phase change on a metallic rose petal RP (AVI)

Video S6. Optical Microscopy video of the dynamics of condensation phase change on a metallic rose petal coated with polydimethylsiloxane (PDMS) RP_{PDMS} (AVI)

Video S7. Optical Microscopy video of the dynamics of condensation phase change on a metallic lotus leaf LL (AVI)

Video S8. Optical Microscopy video of the dynamics of condensation phase change on a metallic lotus leaf coated with polydimethylsiloxane (PDMS) LL_{PDMS} (AVI)

AUTHOR INFORMATION

Corresponding Author

*Authors to whom correspondence should be addressed.

*E-mail to Daniel Orejon: d.orejon@ed.ac.uk & orejon.daniel@heat.mech.kyushu-u.ac.jp.

ORCID

Daniel Orejon: 0000-0003-1037-5036

Alexandros Askounis: 0000-0003-0813-7856

Daniel Attinger: 0000-0002-2382-1149

Author Contributions

D.A. and Y.T. conceived the idea. D.O. performed condensation experimental observations by optical microscopy and at the macro-scale. D.O. performed additional advancing contact angle measurements and surface chemistry characterization at different exposure times. D.O. analysed all the experimental data, proposed the energy analysis and wrote the paper. A.A. performed SEM, contact angle characterization of the samples as per received, and preliminary condensation experimental observations at the macro-scale. All authors commented on the paper.

Notes

The authors declare no competing financial interests

ACKNOWLEDGMENTS

D.O, A.A. and Y.T. acknowledge the support received from the International Institute for Carbon-Neutral Energy Research (WPI-I^{2}CNER) and the Ministry of Education, Culture, Sports, Science and Technology (MEXT). D.O. acknowledges the support received by the Japanese Society for the Promotion of Science (JSPS) KAKENHI (Grant No. JP16K18029 and JP18K13703). D.A. thanks the Fellowship received by the Japanese Society for the Promotion of Science (JSPS) enabling him to establish this collaboration. The authors acknowledge Dr. Sumitomo Hidaka from Kyushu University for his help and assistance on the environmental setup. The authors acknowledge Dr. Roman Selyanchyn and Dr. Miho Ariyoshi from the International Institute for Carbon-Neutral Energy Research (WPI-I^{2}CNER) and Kyushu University for their assistance on sample cleaning by oxygen plasma.

REFERENCES

1. Beér, J. M., High Efficiency Electric Power Generation: The Environmental Role. *Progress in Energy and Combustion Science* **2007,** *33* (2), 107-134.
2. Carey, V. P., *Liquid Vapor Phase Change Phenomena: An Introduction to the Thermophysics of Vaporization and Condensation Processes in Heat Transfer Equipment, Second Edition*. Taylor & Francis: **2007**.
3. Khawaji, A. D.; Kutubkhanah, I. K.; Wie, J.-M., Advances in Seawater Desalination Technologies. *Desalination* **2008,** *221* (1), 47-69.
4. Parker, A. R.; Lawrence, C. R., Water Capture by a Desert Beetle. *Nature* **2001,** *414*, 33-34.
5. Enright, R.; Miljkovic, N.; Alvarado, J. L.; Kim, K.; Rose, J. W., Dropwise Condensation on Micro- and Nanostructured Surfaces. *Nanoscale and Microscale Thermophysical Engineering* **2014,** *18* (3), 223-250.
6. Miljkovic, N.; Enright, R.; Nam, Y.; Lopez, K.; Dou, N.; Sack, J.; Wang, E. N., Jumping-Droplet-Enhanced Condensation on Scalable Superhydrophobic Nanostructured Surfaces. *Nano Letters* **2013,** *13* (1), 179-187.
7. Rose, J. W., Dropwise Condensation Theory and Experiment: A Review. *Proceedings of the Institution of Mechanical Engineers, Part A: Journal of Power and Energy* **2002,** *216* (2), 115-128.
8. Westwater, J. W., Gold surfaces for condensation heat transfer. *Gold Bulletin* **1981,** *14* (3), 95-101.
9. Azimi, G.; Dhiman, R.; Kwon, H.-M.; Paxson, A. T.; Varanasi, K. K., Hydrophobicity of Rare-Earth Oxide Ceramics. *Nature Materials* **2013,** *12*, 315-320.
10. Yan, X.; Huang, Z.; Sett, S.; Oh, J.; Cha, H.; Li, L.; Feng, L.; Wu, Y.; Zhao, C.; Orejon, D.; Chen, F.; Miljkovic, N., Atmospheric-Mediated Superhydrophobicity of Rationally Designed Micro/Nanostructured Surfaces. *ACS Nano* **2019,** *13* (4), 4160-4173.
11. Wilke, K. L.; Preston, D. J.; Lu, Z.; Wang, E. N., Toward Condensation-Resistant Omniphobic Surfaces. *ACS Nano* **2018,** *12* (11), 11013-11021.
12. Le Fevre, E. J.; Rose, J. W., An Experimental Study of Heat Transfer by Dropwise Condensation. *International Journal of Heat and Mass Transfer* **1965,** *8* (8), 1117-1133.
13. Graham, C.; Griffith, P., Drop Size Distributions and Heat Transfer in Dropwise Condensation. *International Journal of Heat and Mass Transfer* **1973,** *16* (2), 337-346.
14. Parin, R.; Martucci, A.; Sturaro, M.; Bortolin, S.; Bersani, M.; Carraro, F.; Del Col, D., Nano-Structured Aluminum Surfaces for Dropwise Condensation. *Surface and Coatings Technology* **2018,** *348*, 1-12.
15. Attinger, D.; Frankiewicz, C.; Betz, A. R.; Schutzius, T. M.; Ganguly, R.; Das, A.; Kim, C.-J.; Megaridis, C. M., Surface Engineering for Phase Change Heat Transfer: A Review. *MRS Energy & Sustainability* **2014,** *1* (E4), 1-40.
16. Ghosh, A.; Beaini, S.; Zhang, B. J.; Ganguly, R.; Megaridis, C. M., Enhancing Dropwise Condensation through Bioinspired Wettability Patterning. *Langmuir* **2014,** *30* (43), 13103-13115.
17. Orejon, D.; Shardt, O.; Gunda, N. S. K.; Ikuta, T.; Takahashi, K.; Takata, Y.; Mitra, S. K., Simultaneous Dropwise and Filmwise Condensation on Hydrophilic Microstructured Surfaces. *International Journal of Heat and Mass Transfer* **2017,** *114*, 187-197.
18. Oh, J.; Zhang, R.; Shetty, P. P.; Krogstad, J. A.; Braun, P. V.; Miljkovic, N., Thin Film Condensation on Nanostructured Surfaces. *Advanced Functional Materials* **2018,** *28* (16), 1707000, 1-10.
19. Chavan, S.; Cha, H.; Orejon, D.; Nawaz, K.; Singla, N.; Yeung, Y. F.; Park, D.; Kang, D. H.; Chang, Y.; Takata, Y.; Miljkovic, N., Heat Transfer through a Condensate Droplet on Hydrophobic and Nanostructured Superhydrophobic Surfaces. *Langmuir* **2016,** *32* (31), 7774-7787.
20. Boreyko, J. B.; Chen, C.-H., Self-Propelled Dropwise Condensate on Superhydrophobic Surfaces. *Physical Review Letters* **2009,** *103* (18), 184501, 1-4.

21. Xuemei, C.; Jun, W.; Ruiyuan, M.; Meng, H.; Nikhil, K.; Shuhuai, Y.; Zuankai, W., Nanograssed Micropyramidal Architectures for Continuous Dropwise Condensation. *Advanced Functional Materials* **2011,** *21* (24), 4617-4623.
22. Lv, C.; Hao, P.; Zhang, X.; He, F., Dewetting Transitions of Dropwise Condensation on Nanotexture-Enhanced Superhydrophobic Surfaces. *ACS Nano* **2015,** *9* (12), 12311-12319.
23. Sharma, C. S.; Combe, J.; Giger, M.; Emmerich, T.; Poulikakos, D., Growth Rates and Spontaneous Navigation of Condensate Droplets Through Randomly Structured Textures. *ACS Nano* **2017,** *11* (2), 1673-1682.
24. Wen, R.; Lan, Z.; Peng, B.; Xu, W.; Yang, R.; Ma, X., Wetting Transition of Condensed Droplets on Nanostructured Superhydrophobic Surfaces: Coordination of Surface Properties and Condensing Conditions. *ACS Applied Materials & Interfaces* **2017,** *9* (15), 13770-13777.
25. Cha, H.; Xu, C.; Sotelo, J.; Chun, J. M.; Yokoyama, Y.; Enright, R.; Miljkovic, N., Coalescence-Induced Nanodroplet Jumping. *Physical Review Fluids* **2016,** *1* (6), 064102, 1-18.
26. Mulroe, M. D.; Srijanto, B. R.; Ahmadi, S. F.; Collier, C. P.; Boreyko, J. B., Tuning Superhydrophobic Nanostructures To Enhance Jumping-Droplet Condensation. *ACS Nano* **2017,** *11* (8), 8499-8510.
27. Bonner III, R. W. In *Dropwise Condensation Life Testing of Self Assembled Monolayers*, Proceedings of the 14th International Heat Transfer Conference, IHTC14-22936, Washington, DC, USA, **2010**; pp 221-226.
28. Cho, H. J.; Preston, D. J.; Zhu, Y.; Wang, E. N., Nanoengineered Materials for Liquid–Vapour Phase-Change Heat Transfer. *Nature Reviews Materials* **2016,** *2*, 16092, 1-17.
29. Mortazavi, V.; Khonsari, M. M., On the Degradation of Superhydrophobic Surfaces: A Review. *Wear* **2017,** *372-373*, 145-157.
30. Ju, J.; Zheng, Y.; Jiang, L., Bioinspired One-Dimensional Materials for Directional Liquid Transport. *Accounts of Chemical Research* **2014,** *47* (8), 2342-2352.
31. Schirhagl, R.; Weder, C.; Lei, J.; Werner, C.; Textor, H. M., Bioinspired Surfaces and Materials. *Chemical Society Reviews* **2016,** *45* (2), 234-236.
32. Zhu, H.; Guo, Z.; Liu, W., Biomimetic Water-Collecting Materials Inspired by Nature. *Chemical Communications* **2016,** *52* (20), 3863-3879.
33. Qin, D.; Xia, Y.; Whitesides, G. M., Soft Lithography for Micro- and Nanoscale Patterning. *Nature Protocols* **2010,** *5*, 491-502.
34. Sharma, V.; Orejon, D.; Takata, Y.; Krishnan, V.; Harish, S., Gladiolus dalenii Based Bioinspired Structured Surface via Soft Lithography and Its Application in Water Vapor Condensation and Fog Harvesting. *ACS Sustainable Chemistry & Engineering* **2018,** *6* (5), 6981-6993.
35. Koch, K.; Bhushan, B.; Jung, Y. C.; Barthlott, W., Fabrication of Artificial Lotus Leaves and Significance of Hierarchical Structure for Superhydrophobicity and Low Adhesion. *Soft Matter* **2009,** *5* (7), 1386-1393.
36. Wang, R.; Zhu, J.; Meng, K.; Wang, H.; Deng, T.; Gao, X.; Jiang, L., Bio-Inspired Superhydrophobic Closely Packed Aligned Nanoneedle Architectures for Enhancing Condensation Heat Transfer. *Advanced Functional Materials* **2018,** *28* (49), 1800634, 1-8.
37. Wang, G.; Zhang, T.-Y., Oxygen Adsorption Induced Superhydrophilic-to-Superhydrophobic Transition on Hierarchical Nanostructured CuO Surface. *Journal of Colloid and Interface Science* **2012,** *377* (1), 438-441.
38. Yin, K.; Du, H.; Dong, X.; Wang, C.; Duan, J.-A.; He, J., A Simple Way to Achieve Bioinspired Hybrid Wettability Surface with Micro/Nanopatterns for Efficient Fog Collection. *Nanoscale* **2017,** *9* (38), 14620-14626.
39. Zhang, L.; Wu, J.; Hedhili, M. N.; Yang, X.; Wang, P., Inkjet Printing for Direct Micropatterning of a Superhydrophobic Surface: Toward Biomimetic Fog Harvesting Surfaces. *Journal of Materials Chemistry A* **2015,** *3* (6), 2844-2852.
40. Thickett, S. C.; Neto, C.; Harris, A. T., Biomimetic Surface Coatings for Atmospheric Water Capture Prepared by Dewetting of Polymer Films. *Advanced Materials* **2011,** *23* (32), 3718-3722.

41. Liu, S.; Latthe, S. S.; Yang, H.; Liu, B.; Xing, R., Raspberry-like superhydrophobic silica coatings with self-cleaning properties. *Ceramics International* **2015,** *41* (9, Part B), 11719-11725.
42. Latthe, S. S.; Sutar, R. S.; Kodag, V. S.; Bhosale, A. K.; Kumar, A. M.; Kumar Sadasivuni, K.; Xing, R.; Liu, S., Self – cleaning superhydrophobic coatings: Potential industrial applications. *Progress in Organic Coatings* **2019,** *128*, 52-58.
43. Bellanger, H.; Darmanin, T.; Taffin de Givenchy, E.; Guittard, F., Chemical and Physical Pathways for the Preparation of Superoleophobic Surfaces and Related Wetting Theories. *Chemical Reviews* **2014,** *114* (5), 2694-2716.
44. Frankiewicz, C.; Attinger, D., Texture and Wettability of Metallic Lotus Leaves. *Nanoscale* **2016,** *8* (7), 3982-3990.
45. Liu, S.; Liu, X.; Latthe, S. S.; Gao, L.; An, S.; Yoon, S. S.; Liu, B.; Xing, R., Self-cleaning transparent superhydrophobic coatings through simple sol–gel processing of fluoroalkylsilane. *Applied Surface Science* **2015,** *351*, 897-903.
46. Preston, D. J.; Miljkovic, N.; Sack, J.; Enright, R.; Queeney, J.; Wang, E. N., Effect of Hydrocarbon Adsorption on the Wettability of Rare Earth Oxide Ceramics. *Applied Physics Letters* **2014,** *105* (1), 011601, 1-5.
47. Lundy, R.; Byrne, C.; Bogan, J.; Nolan, K.; Collins, M. N.; Dalton, E.; Enright, R., Exploring the Role of Adsorption and Surface State on the Hydrophobicity of Rare Earth Oxides. *ACS Applied Materials & Interfaces* **2017,** *9* (15), 13751-13760.
48. Chang, F.-M.; Cheng, S.-L.; Hong, S.-J.; Sheng, Y.-J.; Tsao, H.-K., Superhydrophilicity to Superhydrophobicity Transition of CuO Nanowire Films. *Applied Physics Letters* **2010,** *96* (11), 114101, 1-3.
49. Shirazy, M. R. S.; Blais, S.; Fréchette, L. G., Mechanism of Wettability Transition in Copper Metal Foams: From Superhydrophilic to Hydrophobic. *Applied Surface Science* **2012,** *258* (17), 6416-6424.
50. Yan, X.; Chen, F.; Sett, S.; Feng, L.; Oh, J.; Cha, H.; Li, L.; Huang, Z.; Miljkovic, N. In *Coalescence-Induced Droplet Jumping on Atmospheric-Mediated Superhydrophobic Surfaces*, Proceedings of the 16th International Heat Transfer Conference, IHTC-16-22157, Beijing, China, **2018**; pp 1-8.
51. Bhushan, B.; Her, E. K., Fabrication of Superhydrophobic Surfaces with High and Low Adhesion Inspired from Rose Petal. *Langmuir* **2010,** *26* (11), 8207-8217.
52. Ensikat, H. J.; Ditsche-Kuru, P.; Neinhuis, C.; Barthlott, W., Superhydrophobicity in Perfection: the Outstanding Properties of the Lotus Leaf. *Beilstein Journal of Nanotechnology* **2011,** *2*, 152-161.
53. Gao, X.; Zhou, J.; Du, R.; Xie, Z.; Deng, S.; Liu, R.; Liu, Z.; Zhang, J., Robust Superhydrophobic Foam: A Graphdiyne‐Based Hierarchical Architecture for Oil/Water Separation. *Advanced Materials* **2016,** *28* (1), 168-173.
54. Yuan, J.; Liu, X.; Akbulut, O.; Hu, J.; Suib, S. L.; Kong, J.; Stellacci, F., Superwetting nanowire membranes for selective absorption. *Nature Nanotechnology* **2008,** *3*, 332.
55. Bhushan, B.; Nosonovsky, M., The Rose Petal Effect and the Modes of Superhydrophobicity. *Philosophical Transactions of the Royal Society A: Mathematical, Physical and Engineering Sciences* **2010,** *368* (1929), 4713-4728.
56. Bhushan, B.; Jung, Y. C.; Koch, K., Micro-, Nano- and Hierarchical Structures for Superhydrophobicity, Self-Cleaning and Low Adhesion. *Philosophical Transactions of the Royal Society A: Mathematical, Physical and Engineering Sciences* **2009,** *367* (1894), 1631-1672.
57. Zhang, P.; Maeda, Y.; Lv, F.; Takata, Y.; Orejon, D., Enhanced Coalescence-Induced Droplet-Jumping on Nanostructured Superhydrophobic Surfaces in the Absence of Microstructures. *ACS Applied Materials & Interfaces* **2017,** *9* (40), 35391-35403.
58. ImageJ, I. b. W. R., National Institutes of Health, USA, last checked: April 2016, URL http://imagej.nih.gov/ij.
59. Ölçeroğlu, E.; McCarthy, M., Self-Organization of Microscale Condensate for Delayed Flooding of Nanostructured Superhydrophobic Surfaces. *ACS Applied Materials & Interfaces* **2016,** *8* (8), 5729-5736.

60. Schrader, M. E., Young-Dupre Revisited. *Langmuir* **1995,** *11* (9), 3585-3589.
61. Lv, C.; Hao, P.; Yao, Z.; Song, Y.; Zhang, X.; He, F., Condensation and Jumping Relay of Droplets on Lotus Leaf. *Applied Physics Letters* **2013,** *103* (2), 021601, 1-5.
62. Whyman, G.; Bormashenko, E.; Stein, T., The Rigorous Derivation of Young, Cassie–Baxter and Wenzel Equations and the Analysis of the Contact Angle Hysteresis Phenomenon. *Chemical Physics Letters* **2008,** *450* (4), 355-359.
63. Kita, Y.; Mackenzie Dover, C.; Askounis, A.; Takata, Y.; Sefiane, K., Drop Mobility on Superhydrophobic Microstructured Surfaces with Wettability Contrasts. *Soft Matter* **2018,** *14* (46), 9418-9424.
64. Wenzel, R. N., Resistance of Solid Surfaces to Wetting by Water. *Industrial & Engineering Chemistry* **1936,** *28* (8), 988-994.
65. Miljkovic, N.; Enright, R.; Wang, E. N., Effect of Droplet Morphology on Growth Dynamics and Heat Transfer during Condensation on Superhydrophobic Nanostructured Surfaces. *ACS Nano* **2012,** *6* (2), 1776-1785.
66. Liu, T.; Sun, W.; Li, X.; Sun, X.; Ai, H., Growth Modes of Condensates on Nano-Textured Surfaces and Mechanism of Partially Wetted Droplet Formation. *Soft Matter* **2013,** *9* (41), 9807-9815.
67. Chen, X.; Patel, R. S.; Weibel, J. A.; Garimella, S. V., Coalescence-Induced Jumping of Multiple Condensate Droplets on Hierarchical Superhydrophobic Surfaces. *Scientific Reports* **2016,** *6*, 18649, 1-11.
68. Chen, X.; Ma, R.; Li, J.; Hao, C.; Guo, W.; Luk, B. L.; Li, S. C.; Yao, S.; Wang, Z., Evaporation of Droplets on Superhydrophobic Surfaces: Surface Roughness and Small Droplet Size Effects. *Physical Review Letters* **2012,** *109* (11), 116101, 1-6.
69. Cassie, A. B. D.; Baxter, S., Wettability of Porous Surfaces. *Transactions of the Faraday Society* **1944,** *40* (0), 546-551.
70. Enright, R.; Miljkovic, N.; Dou, N.; Nam, Y.; Wang, E. N., Condensation on Superhydrophobic Copper Oxide Nanostructures. *Journal of Heat Transfer* **2013,** *135* (9), 091304-091304, 1-12.
71. Rose, J. W.; Glicksman, L. R., Dropwise Condensation—The Distribution of Drop Sizes. *International Journal of Heat and Mass Transfer* **1973,** *16* (2), 411-425.
72. Rose, J. W., Further Aspects of Dropwise Condensation Theory. *International Journal of Heat and Mass Transfer* **1976,** *19* (12), 1363-1370.
73. Weisensee, P. B.; Wang, Y.; Hongliang, Q.; Schultz, D.; King, W. P.; Miljkovic, N., Condensate Droplet Size Distribution on Lubricant-Infused Surfaces. *International Journal of Heat and Mass Transfer* **2017,** *109* (Supplement C), 187-199.
74. Frankiewicz, C.; Attinger, D., On Temporal Biphilicity: Definition, Relevance, and Technical Implementation in Boiling Heat Transfer. *Journal of Heat Transfer* **2017,** *139* (11), 111511, 1-14.
75. Yao, X.; Chen, Q.; Xu, L.; Li, Q.; Song, Y.; Gao, X.; Quéré, D.; Jiang, L., Bioinspired Ribbed Nanoneedles with Robust Superhydrophobicity. *Advanced Functional Materials* **2010,** *20* (4), 656-662.

TOC

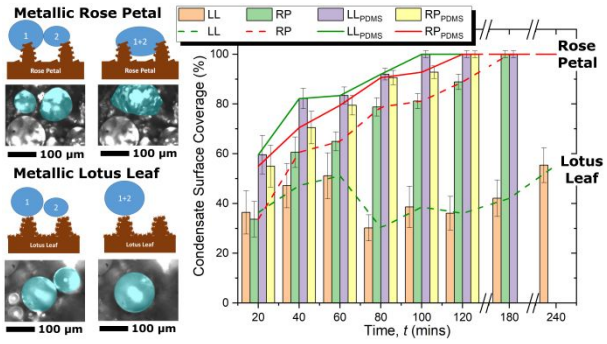
Metallic Rose Petal
100 µm
100 µm
Metallic Lotus Leaf
100 µm
100 µm
LL
RP
LL$_{PDMS}$
RP$_{PDMS}$
Condensate Surface Coverage (%)
Time, t (mins)
Rose Petal
Lotus Leaf